Dynamic modelling and analysis of cracked gear system with tip relief based on proposed variable-angle deformation energy integration method

Lantao Yang[1, 2], Desheng Zou[1], Xiuquan Sun[2], Liming Wang[1], Yimin Shao[1*], Fengshou Gu[2], Andrew Ball[2], David Mba[3]

[1] State Key Laboratory of Mechanical Transmission, Chongqing University, Chongqing 400044, China

[2] Centre for Efficiency and Performance Engineering, University of Huddersfield, Huddersfield HD1 3DH, UK

[3] Creative Computing Institute, University of the Arts London, London WC1V 7EY, UK

[*]Corresponding author. E-mail address: ymshao@cqu.edu.cn

Abstract: Due to ignoring the effects of the change of the tooth attachment position caused by the cracks, traditional time vary mesh stiffness (TVMS) calculation models and dynamic simulations for cracked gears will lose their precision in the body crack case. To address this shortcoming, a new analytical TVMS calculation model of cracked gear considering tip relief (TR) is developed based on a proposed variable-angle deformation energy integration (VADEI) method. On this basis, a dynamic model of the gear system for the analysis of fault vibration characteristics is established. The effectiveness and accuracy of the proposed TVMS calculation model are verified by the finite element (FE) method. A comprehensive investigation is finally carried out to reveal the effects of the parameters of TR, load and crack on the TVMS and dynamic characteristics of the cracked gears. The study results indicate that the proposed models can meet the accurate TVMS calculation and dynamic simulation for both the tooth and body cracked gears, and the influences of the tooth attachment position change caused by the crack can not be ignored. This study could provide a systematic methodology and meaningful reference for the dynamic modelling, simulation and fault diagnosis of gear systems with crack failures.

Keywords: Gear fault diagnosis; Dynamic model; Mesh stiffness; Body crack; Tip relief

List of symbols	
subscript i	Subscript i = 1, 2, 3 represents Zone *I* (i = 1), *II* (i = 2) or *III* (i = 3), respectively
subscript λ	Subscript $\lambda = p, g$ represents driving gear ($\lambda = p$) or driven gear ($\lambda = g$), respectively
α_1	The angle of the meshing force
α_2	Half of the tooth angle corresponding to the base circle
α_p	The included angle of the action line and the x coordinate in the fixed coordinate system in Fig. 8
A_{xi}	The area of the micro-section dx_i
$c_{\lambda x}/c_{\lambda y}$	Bearing damping of gear λ in x/y direction
c_m	Total meshing damping
C_n	Amount of tooth TR
d_1	The horizontal distance between the meshing position and the intersection of tooth profile and base circle
d_2	The horizontal distance between the intersections of tooth profile with dedendum circle and base circle

d_3	The horizontal distance between the crack tip and the intersection of tooth profile and dedendum circle
e_{pg}	The relative error excitation displacement of the driven gear relative to the driving gear
$\dot{e}_{pg}$	The relative error excitation velocity of the driven gear relative to the driving gear
E	Gear elasticity modulus
E_{kj}	The relative profile error of any tooth pair j relative to the maximum deformation tooth pair k
$E_{\lambda j}/E_{\lambda k}$	The tooth profile error of gear λ of any tooth pair j or the maximum deformation tooth pair k
F	Meshing force
F_n	Normal force
F_{ai}/F_{bi}	Axial compression/shear force decomposed by F corresponding to the micro-section dx_i
f_r	Rotation frequency of driving gear
f_m	Meshing frequency
G	Shear modulus of gear
$h_{F(xi)}$	The effective moment arm of F_{ai} on the micro-section dx_i
h_r	The vertical distance between the intersections of the addendum circle and tooth profile and the centerline of the gear tooth
h_{x3}	The length of the effective micro-section dx_3 in Zone *III*
I_{xi}	Area of inertia of the micro-section dx_i
J_λ	Rotational inertia of gear λ
k_m	Total TVMS modified by the tooth errors
K	TVMS of single tooth pair
$K_b/K_s/K_a/K_f$	Stiffness of bending/shear/axial compression/fillet foundation
$K_{b\lambda}/K_{s\lambda}/K_{a\lambda}/K_{f\lambda}$	Stiffness of bending/shear/axial compression/fillet foundation of gear λ
K_{fFEM}	TVMS of single tooth pair calculated by the FE model
K_h	Hertz contact stiffness
$k_{\lambda x}/k_{\lambda y}$	Bearing stiffness of gear λ in the x/y direction
l	The effective moment arm of F_{b3} on the micro-section dx_3
L_n	Length of tooth TR
m	Module of gear
m_λ	Mass of gear λ
M_i	Total bending moment of the micro-section dx_i
n	The first (n = 1) and second (n = 2) tooth pair
p_a	Principal stress p_a of the beam section *NN* in Fig. 3 (a)
q	Crack depth
R_b	Base circle radius
$R_{b\lambda}$	Base circle radius of gear λ
R_g	Dedendum circle radius
R_o	Addendum circle radius
T_r	Rotation period of the driving gear
T_λ	Torque of gear λ

$U_b/U_s/U_a$	Deformation energy of bending/shear/axial compression
W	Tooth width
x_i	Distance of the effective micro-section dx_i from the base circle (i = 1 or 2) or dedendum circle (i = 3)
$x_\lambda / \dot{x}_\lambda / \ddot{x}_\lambda$	Lateral displacement/velocity/acceleration of gear λ along the x-direction
$y_\lambda / \dot{y}_\lambda / \ddot{y}_\lambda$	Lateral displacement/velocity/acceleration of gear λ along the y-direction
$\theta_\lambda / \dot{\theta}_\lambda / \ddot{\theta}_\lambda$	Angular displacement/velocity/acceleration of gear λ
β	F decomposition angle for the effective micro-section dx_3 in Zone *III*
δ_j	Tooth deformation of the jth tooth pairs
δ_λ	The meshing point displacement of gear λ along the line of action
θ	Position angle of the effective micro-section dx_3 in Zone *III*
θ_f	Half of the tooth angle corresponding to the dedendum circle
φ	Crack initiation position angles
ϕ	Meshing position ϕ
τ_a	The shear stress of the beam section *NN* in Fig. 3 (a)
σ_a	The tensile stress of the beam section *NN* in Fig. 3 (a)
v	Crack angle
ω_λ	Rotation speed of gear λ

1. Introduction

The gear system is an important part of mechanical equipment, which is widely used as the key component of power and motion transmission in aerospace, energy development, industrial production and other modern mechanical equipment [1-3]. As one of the important basic components of the gear system, gear often produces crack failures in the operation of the system due to excessive load, improper assembly or fatigue caused by long-term operation [4-5]. The internal excitation of gear will be changed once the crack occurs, which will further affect the dynamic characteristics of the gear system. Therefore, establishing an accurate internal excitation calculation model of cracked gear and then simulating its fault vibration characteristics have become necessary and effective means for scholars to develop fault diagnosis and monitoring methods [6-7].

TVMS is one of the main internal excitation forms of gear systems. Establishing the accurate TVMS calculation model is the primary premise for gear dynamic simulations. At present, the computational methods of TVMS mainly include the analytical method [8-9], FE method [10-12], analytical-FE method [13-15] and experimental method [16-17]. The experimental method is more consistent with the actual situation, but its cost is higher and efficiency is relatively lower. The FE and analytical-FE methods require high-quality mesh division to obtain more accurate results, which are time-consuming and inefficient. In contrast, the analytical method has attracted a lot of attention and is widely adopted by scholars due to its higher computing efficiency and accuracy [19-20].

According to the crack propagation path, gear crack can be divided into two types: tooth crack and body crack [21-22], which are shown in Fig. 1. At present, analytical TVMS calculation methods for cracked gear mainly focus on the tooth crack case. The existing tooth crack models all assumed that the main reason for the decrease of TVMS caused by crack is that the crack reduces

the effective bearing tooth thickness of gear teeth. Therefore, scholars paid more attention to the influence of the factors that affect the effective tooth thickness on the TVMS of cracked gear, such as different crack propagation paths, crack angles and depths, as well as the limiting line of the effective thickness of cracked teeth. For example, the initial TVMS calculation models of crack gears simplified both the crack propagation path and the limiting line as a straight line to study the influence of crack parameters on TVMS [23-25]. Then, Mohammed et al. [26] modified the original TVMS computing model using a parabola between the tooth tip and the crack vertex as the limiting line. Chen et al. [27] replaced the parabolic limiting line with a straight one to limit the effective tooth thickness, achieving the same computational accuracy but simplifying the modelling process. Ma et al. [28] used parabola and straight line to simulate the crack growth path and the limiting line. Considering the early cracks did not run through the whole tooth width, and thus the weakening degree of the crack on tooth thickness is different along with the direction of tooth width, Chen and Shao [29] proposed the slicing method to address the TVMS computing of such cracked gears. In the above models, the cracked tooth is usually assumed to be a non-uniform cantilever beam, and the attachment position of the cracked tooth beam is always on the dedendum circle, and only the attachment area decreases gradually with the crack propagating along the direction of the tooth thickness. However, the attachment position of the cracked tooth cantilever beam actually depends on the position of the crack tip, that is, the attachment position of the cracked tooth will deviate from the root circle as the crack tip extends inside the gear body, then resulting in lengthening and tilting of the tooth cantilever beam [30]. This effect will inevitably affect the TVMS of cracked gear, while it is not considered in the traditional models. This influence will become significant when the crack expands inside the gear body, which will make the traditional TVMS calculation model no longer applicable.

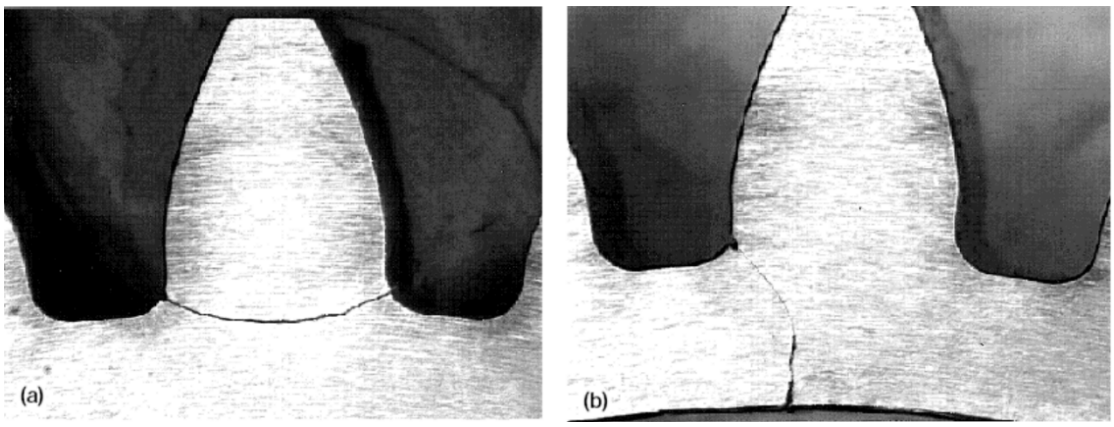

Fig. 1 Crack propagation paths [21-22]: (a) tooth crack, (b) body crack

At present, the analytical TVMS calculation models for gears with body cracks are still lacking [31-32]. Early on, Zhou et al. [33] proposed one analytical TVMS calculation model that can be used in the body crack case, which is the so-called semi-planar cantilever beam model. In Zhou's model, the attachment position of the cracked tooth cantilever beam changes from the dedendum circle in the traditional model to the position of the half gear body. However, taking half of the gear body as a part of the cantilever beam is not consistent with the ideal cantilever beam hypothesis, which will produce larger results than the actual situation [34]. At present, the accurate TVMS calculation model of body cracked gear mainly relies on the FE method [35], which will inevitably lead to low computational efficiency and high cost. Therefore, it is of great

necessity to develop a high-precision and low-cost analytical TVMS calculation model for body cracked gears.

Besides the TVMS excitation, transmission error is also one of the most important internal excitation forms of gears. To reduce the corner contact impact caused by the transmission error, tooth TR is often carried out during the gear machining and manufacturing processes. In the traditional gear dynamic simulation, the tooth error affects the gear dynamics only as a kind of displacement excitation form [36-37]. In 2013, Chen [38] proposed that there is also a coupling effect between the transmission error and TVMS, and presented the TVMS calculation model coupled with tooth errors. In Chen's study, some suggestions were put forward that the tooth TR and load should be considered in the simulation of gear tooth crack since the corner contact is more prone to occur in a cracked gear [38]. At present, the effects of TR and load on the characteristics of internal excitation and dynamic response of the crack faults, especially for the body crack are still unclear and need to be further clarified.

From the above review, several problems still need to be addressed in the TVMS calculation and dynamic modelling of the spur gear with crack fault:

1) The traditional analytical TVMS calculation model of tooth cracked gears mainly concerns the influence of effective tooth thickness reduction caused by the crack on TVMS, but ignores the effect of the change of the cracked tooth attachment position, which makes it no longer applicable to the body crack case. High-precision analytical TVMS calculation models of gears with body crack failures are extremely scarce at present.

2) The differences in the TVMS excitation and dynamic characteristics between the tooth cracked and body cracked gears are not fully clarified.

3) The effects of TR and load on the characteristics of TVMS excitation and dynamic response of the crack faults, especially for the body crack fault are still unclear and need to be further revealed.

Therefore, the aims and contents of the current paper are as follows: By considering the influences of TR and the changes in tooth attachment position caused by the crack, to propose a new analytical TVMS calculation model of cracked gear that can be used for both the tooth and body crack cases. Based on verifying the effectiveness and accuracy of the proposed model, to reveal the effects of the parameters of TR, load and crack on the TVMS excitation of the tooth and body cracked gears. Through establishing a dynamic model of the gear system, to investigate the vibration characteristics of the gear system under both the tooth and body crack cases, and then provide some theoretical basis for the fault type identifying and fault degree evaluation of gear cracks.

The rest of the paper is structured as follows: The developed new analytical TVMS calculation model of cracked gear is introduced in Section 2. The parameters definition of tooth TR and the TVMS calculation process of the proposed model are described in Section 3. The established FE models for validating the correctness and accuracy of the proposed analytical TVMS calculation model are displayed in Section 4. The founded dynamics model of the gear system for exploring the crack fault vibration characteristics is illustrated in Section 5. Then the results obtained from the proposed models are discussed and analyzed in Section 6. Finally, some key conclusions are summarized and listed in Section 7.

2. Proposed TVMS calculation model of gear with crack failure

2.1 Problem formulation

Fig. 2 (a) shows the existing TVMS calculation physical model of the healthy gear, in which the gear tooth is simplified as a variable section cantilever beam attached to the dedendum circle, and the attachment position is the vertical line of the two intersections of the dedendum circle and tooth profile. The stiffness of the healthy gear tooth can be obtained by calculating the deformation of Zone *I* (brown shaded part) and Zone *II* (blue shaded part) under the meshing force *F*. Nevertheless, the effective bearing tooth thickness and attachment area of the gear tooth will change accordingly when a crack appears, leading to the stiffness calculation model of healthy gear being no longer applicable.

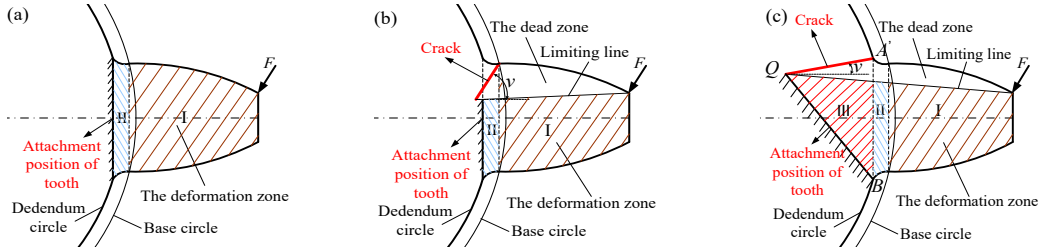

Fig. 2 Different tooth cantilever beam models: (a) healthy tooth model, (b) traditional crack tooth model, (c) proposed tooth gear model

As presented in Fig. 2 (b), the limiting line is adopted in the traditional crack model to calibrate the effective tooth thickness and tooth attachment area of the cracked tooth, that is, the effective tooth thickness and attachment area of the cracked tooth will decrease with the crack propagation. Then the tooth stiffness of the cracked gear can be obtained by calculating the deformation of effective tooth thickness in Zone *I* and Zone *II*. It is worth noting that in the traditional cracked gear model, the tooth attachment position is always on the vertical line at the two intersections of the dedendum circle and tooth profile, and the crack only changes the effective tooth attachment area. The traditional crack model is widely used to compute the TVMS of tooth crack gears, i.e., the crack angle v (pictured) is large and generally not less than 75° [28].

However, as displayed in Fig. 2 (c), the attachment position of the crack tooth actually depends on the position of the crack tip, that is to say when the crack propagates into the gear body (i.e., the crack growth angle v is small), the crack not only changes the effective bearing tooth thickness and tooth attachment area but also affects the angle of tooth attachment position (denoted with ∠KBQ in the picture) [30]. This change will lengthen the cracked tooth cantilever beam, namely, the zone *III* is also included in the effective deformation zone of the tooth cantilever beam, which makes the cracked tooth model appear as a lengthened and inclined irregular cantilever beam. However, the traditional cracked gear model cannot take into account the effects mentioned above, which is bound to cause calculation errors, especially in the case of body crack (i.e., the crack growth angle v is small).

Therefore, based on the proposed new cantilever beam model of cracked teeth, this section intends to establish a new TVMS calculation model of cracked gear by considering the effects of the tooth attachment position change caused by the crack, then to further improve the accuracy of

the traditional model and provide a new approach for computing the TVMS of the gears with body crack failures.

2.2 Modelling principle

According to the deformation superposition principle of the cantilever beam, the whole tooth deformation can be calculated by the summation of the deformation of Zones *I*, *II* and *III* under the action of meshing force. The tooth stiffness of zones *I* and *II* can be solved according to the traditional stiffness calculation model of cracked gear [39]. Therefore, the key problem to be addressed in this modelling is how to calculate the stiffness of the lengthened and inclined part in the cracked tooth cantilever beam, namely, the tooth stiffness of Zone *III* presented in Fig. 2 (c).

As displayed in Fig. 3 (a), based on the stress decomposition method, the principal stress p_a of the beam section *NN* can be decomposed into a tensile stress σ_a perpendicular to the inclined section and shear stress τ_a parallel to the section according to an inclined angle θ of the cross-section.

Inspired by the force decomposition method presented in Fig. 3 (a), a variable-angle deformation energy integration method is proposed to calculate the deformation energy of the lengthened and inclined tooth zone (Zone *III*). As displayed in Fig. 3 (b), the force decomposition angle β of each inclined micro-section dx_3 in Zone *III* varies with the position angle θ. By integrating the bending, axial compression and shear deformation energy of the inclined micro-section dx_3 from position $x_3 = 0$ to $x_3 = d_3$ (i.e. corresponding angle θ from 0° to ∠KBQ), then the total deformation energy of Zone *III* under each meshing position can be obtained. Finally, the total tooth stiffness of the proposed new cantilever beam model can be calculated based on the energy method [40].

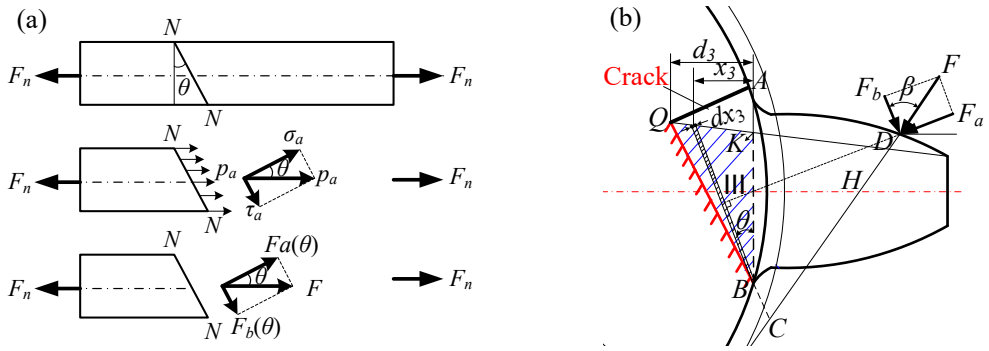

Fig. 3 Proposed modelling principle and method: (a) stress decomposition method of beam cross-section, (b) schematic diagram of the proposed VADEI method

2.3 TVMS calculation modelling for the proposed new crack tooth cantilever beam

The details of the proposed new tooth cantilever beam model of the cracked gear for TVMS calculation modelling are shown in Fig. 4. In this model, the inclined straight limiting line defining the effective thickness of the cracked tooth in Ref. [27] is adopted due to its high accuracy and modelling convenience for both large and small crack cases.

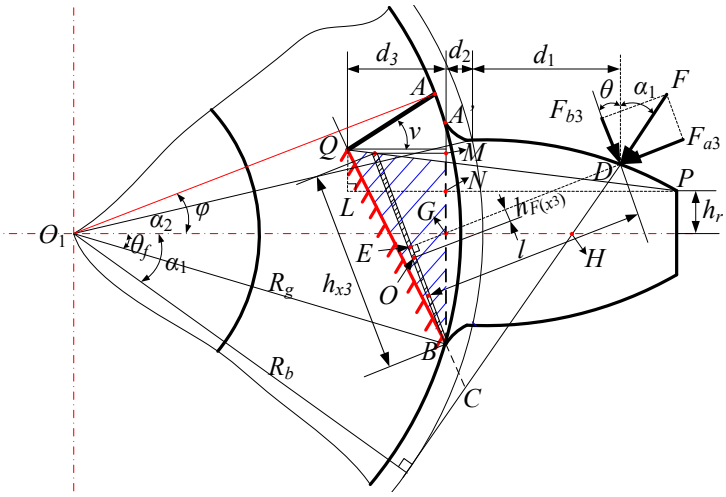

Fig. 4 The proposed new cantilever beam of the cracked tooth

In Fig. 3 (b) and Fig. 4, point A is the crack's initial point, AQ represents the crack, and its depth is equal to q. PQ stands for the limiting line. Points A' and B are the two intersection points of the dedendum circle and tooth profile, point D refers to the meshing point. BQ denotes the new attachment area of the crack tooth cantilever beam, point C is the intersection of the line BQ and the meshing line DC. Points G and H are the two intersection points of the gear tooth centerline with lines $A'B$ and DC, respectively. Points K and N are the intersection points of line $A'B$ with lines PQ and PL subsequently. Point M is the intersection of line $A'B$ with the horizontal line at the top of the micro-section dx_3, point E is the intersection of the action line of the meshing force component F_{a3} and the micro-section dx_3, Point O is the midpoint of the micro-section dx_3.

The bending deformation energy U_b, axial compressive deformation energy U_a and shear deformation energy U_s stored in a loaded gear tooth can be expressed by [40-41],

$$U_b = \frac{F^2}{2K_b},\ U_a = \frac{F^2}{2K_a},\ U_s = \frac{F^2}{2K_s} \tag{1}$$

where K_b, K_a and K_s represent the total tooth stiffness of bending, axial compressive and shear under the meshing load F. The potential energy of the tooth cantilever beam can be also obtained through the beam theory,

$$\begin{cases} U_b = \int_0^{d_1} \frac{M_1^{\,2}}{2EI_{x_1}} dx_1 + \int_0^{d_2} \frac{M_2^{\,2}}{2EI_{x_2}} dx_2 + \int_0^{d_3} \frac{M_3^{\,2}}{2EI_{x_3}} dx_3 \\ U_a = \int_0^{d_1} \frac{F_{a1}^{\,2}}{2EA_{x_1}} dx_1 + \int_0^{d_2} \frac{F_{a2}^{\,2}}{2EA_{x_2}} dx_2 + \int_0^{d_3} \frac{F_{a3}^{\,2}}{2EA_{x_3}} dx_3 \\ U_s = \int_0^{d_1} \frac{1.2F_{b1}^{\,2}}{2GA_{x1}} dx_1 + \int_0^{d_2} \frac{1.2F_{b2}^{\,2}}{2GA_{x_2}} dx_2 + \int_0^{d_3} \frac{1.2F_{b3}^{\,2}}{2GA_{x_3}} dx_3 \end{cases} \tag{2}$$

of which, M_i, I_{xi} and A_{xi} respectively represent the total bending moment, the area of inertia and the area of the micro-section dx_i where the distance from the base circle (when in Zone I and II) or dedendum circle (when in Zone III) is x_i; F_{ai} and F_{bi} refer to the two components of the meshing force F corresponding to the micro-section dx_i. The subscript i = 1, 2, 3 denotes the micro-section in Zone I, II and III, respectively.

Since the angle of meshing force decomposition corresponding to the micro-section in Zone *I* and *II* keeps a constant α_1, there are $F_{a1}= F_{a2}$ and $F_{b1}= F_{b2}$, while in Zone *III*, F_{a3} and F_{b3} differ according to the angle θ of the micro-section dx_3. Thus, F_{ai} and F_{bi} can be expressed as follows,

$$\begin{cases} F_{a1} = F_{a2} = F\sin\alpha_1,\ F_{b1} = F_{b2} = F\cos\alpha_1 \\ F_{a3} = F\sin\beta,\ F_{b3} = F\cos\beta,\ \text{where } \beta = \alpha_1 + \theta \end{cases} \tag{3}$$

Gear crack will be in an open state under the mesh load, which will result in the offset of the neutral axis of the effective tooth thickness [39], that is to say, the bending moment aroused by F_a will no longer be a constant value but a function of x_i (i = 1, 2, 3). Thus, the bending moment in Zone *I*, *II* and *III* can be calculated as follows,

$$M_1 = F_{b1}\cdot\left(d_1 - x_1\right) - F_{a1}\cdot h_{F(x_1)},\ M_2 = F_{b2}\cdot\left(d_1 + x_2\right) - F_{a2}\cdot h_{F(x_2)},\ M_3 = F_{b3}\cdot l - F_{a3}\cdot h_{F(x_3)} \tag{4}$$

Here, $h_{F(xi)}$ means the effective moment arm of F_a on the micro-section dx_i.

Then, according to Eqs. (1)-(4), K_b, K_a and K_s can be expressed separately as,

$$\frac{1}{K_b} = \underbrace{\int_0^{d_1} \frac{\left[\left(d_1 - x_1\right)\cos\alpha_1 - h_{F(x_1)}\sin\alpha_1\right]^2}{EI_{x1}} dx_1}_{\frac{1}{K_{b1}}} + \underbrace{\int_0^{d_2} \frac{\left[\left(d_1 + x_2\right)\cos\alpha_1 - h_{F(x_2)}\sin\alpha_1\right]^2}{EI_{x2}} dx_2}_{\frac{1}{K_{b2}}} + \underbrace{\int_0^{d_3} \frac{\left[l\cos\beta - h_{F(x_3)}\sin\beta\right]^2}{EI_{x3}} dx_3}_{\frac{1}{K_{b3}}} \tag{5}$$

$$\frac{1}{K_a} = \underbrace{\int_0^{d_1} \frac{\sin^2\alpha_1}{EA_{x1}} dx_1}_{\frac{1}{K_{a1}}} + \underbrace{\int_0^{d_2} \frac{\sin^2\alpha_1}{EA_{x2}} dx_2}_{\frac{1}{K_{a2}}} + \underbrace{\int_0^{d_3} \frac{\sin^2\beta}{EA_{x3}} dx_3}_{\frac{1}{K_{a3}}} \tag{6}$$

$$\frac{1}{K_s} = \underbrace{\int_0^{d_1} \frac{1.2\cos^2\alpha_1}{GA_{x1}} dx_1}_{\frac{1}{K_{s1}}} + \underbrace{\int_0^{d_2} \frac{1.2\cos^2\alpha_1}{GA_{x2}} dx_2}_{\frac{1}{K_{s2}}} + \underbrace{\int_0^{d_3} \frac{1.2\cos^2\beta}{GA_{x3}} dx_3}_{\frac{1}{K_{s3}}} \tag{7}$$

In Eqs. (5)-(7), K_{bi}, K_{ai} and K_{si} represent the tooth stiffness of the bending, axial compressive and shear in Zone i, the detailed calculation process of K_{bi}, K_{ai} and K_{si} of Zone *I* and *II* can be found in Ref. [39] and will not repeat here. In this paper, we only focus on the computational modelling of the tooth stiffness of Zone *III*. The parameters d_3, I_{x3}, A_{x3}, $h_{F(x3)}$ and l in Zone *III* can be expressed as,

$$d_3 = q\cos\nu + R_g\cos\theta_f - R_g\cos\varphi \tag{8}$$

$$I_{x3} = \frac{1}{12}{h_{x3}}^3 W \tag{9}$$

$$A_{x3} = h_{x3} W \tag{10}$$

$$l = \left|DC\right|\sin\left(\alpha_1 + \theta\right) \tag{11}$$

$$h_{F(x_3)} = \left|EC\right| - \left|OC\right| \tag{12}$$

Substitute Eqs. (9)-(12) into Eqs. (5)-(7), K_{b3}, K_{a3} and K_{s3} can be written as,

$$\frac{1}{K_{b3}} = \int_0^{d_3} \frac{\left[\left|DC\right|\sin\beta\cos\beta - \left(\left|DC\right|\cos\beta - \left|OC\right|\right)\sin\beta\right]^2}{EI_{x3}} dx_3 = \int_0^{d_3} \frac{12\left[\left|OC\right|\sin\left(\alpha_1 + \theta\right)\right]^2}{EW{h_{x3}}^3} dx_3 \tag{13}$$

$$\frac{1}{K_{a3}}=\int_0^{d_3}\frac{\sin^2(\alpha_1+\theta)}{EWh_{x3}}dx_3 \tag{14}$$

$$\frac{1}{K_{s3}}=\int_0^{d_3}\frac{1.2\cos^2(\alpha_1+\theta)}{GWh_{x3}}dx_3 \tag{15}$$

In Eqs. (13)-(15), the length h_{x3} and the angle θ can be calculated as,

$$h_{x3}=\sqrt{{x_3}^2+|MB|^2} \tag{16}$$

$$\theta=\arctan\left(x_3/|MB|\right) \tag{17}$$

where,

$$|MB|=R_g\sin\theta_f+|NK|+|MK|+h_r \tag{18}$$

of which

$$|NK|=|QL|\frac{|NP|}{|LP|}=\left(R_g\sin\varphi-q\sin\nu-h_r\right)\frac{R_o\cos\alpha_K-R_g\cos\theta_f}{R_o\cos\alpha_K-R_g\cos\theta_f+d_3} \tag{19}$$

$$|MK|=x_3\frac{|QL|}{|LP|}=\frac{x_3\left(R_g\sin\varphi-q\sin\nu-h_r\right)}{R_o\cos\alpha_K-R_g\cos\theta_f+d_3} \tag{20}$$

In Eq. (13), the length of line segment $|OC|$ can be calculated as follows:

The lengths of line segments GH and GB can be deduced by,

$$|GH|=|O_1H|-|O_1G|=R_b/\cos\alpha_1-R_g\cos\theta_f \tag{21}$$

$$|GB|=R_g\sin\theta_f \tag{22}$$

By establishing a rectangular coordinate system with the lines $A'B$ and O_1G as the horizontal and vertical axes respectively, the equation of line DC in this rectangular coordinate system can be obtained,

$$y_{DC}=-\tan\alpha_1\cdot x_{DC}+|GH| \tag{23}$$

And the equation of line EC in the rectangular coordinate system can be deduced as,

$$y_{EC}=\tan\theta\cdot x_{EC}-|GB|\tan\theta \tag{24}$$

Then, by combining Eqs. (23)-(24), the coordinate of point C (x_C, y_C) can be obtained as,

$$\begin{cases}x_C=\dfrac{|GH|+|GB|\tan\theta}{\tan\theta+\tan\alpha_1}\\ y_C=\dfrac{-\tan\alpha_1(|GH|+|GB|\tan\theta)}{\tan\theta+\tan\alpha_1}+|GH|\end{cases} \tag{25}$$

Then the $|BC|$ can be deduced as,

$$|BC|=\sqrt{\left(\frac{|GH|+|GB|\tan\theta}{\tan\theta+\tan\alpha_1}-|GB|\right)^2+\left(\frac{-\tan\alpha_1(|GH|+|GB|\tan\theta)}{\tan\theta+\tan\alpha_1}+|GH|\right)^2} \tag{26}$$

Thus the $|OC|$ can be obtained as,

$$|OC| = |OB| + |BC| = \frac{1}{2}h_{x3} + \sqrt{\left(\frac{|GH| + |GB|\tan\theta}{\tan\theta + \tan\alpha_1} - |GB|\right)^2 + \left(\frac{-\tan\alpha_1(|GH| + |GB|\tan\theta)}{\tan\theta + \tan\alpha_1} + |GH|\right)^2} \quad (27)$$

Substitute Eqs. (16), (17) and (27) into Eqs. (13)-(15), K_{b3}, K_{a3} and K_{s3} can be finally obtained as a function of x_3, which are presented as,

$$\frac{1}{K_{b3}} = \int_0^{d_3} \frac{12\left[\left(\frac{1}{2}h_{x3} + \sqrt{\left(\frac{|GH| + |GB|(x_3/|MB|)}{(x_3/|MB|) + \tan\alpha_1} - |GB|\right)^2 + \left(\frac{-\tan\alpha_1(|GH| + |GB|(x_3/|MB|)}{(x_3/|MB|) + \tan\alpha_1} + |GH|\right)^2}\right)\sin(\alpha_1 + \arctan(x_3/|MB|))\right]^2}{EW\left(\sqrt{x_3^2 + |MB|^2}\right)^3} dx_3 \quad (28)$$

$$\frac{1}{K_{a3}} = \int_0^{d_3} \frac{\sin^2\left[\alpha_1 + \arctan(x_3/|MB|)\right]}{EW\sqrt{x_3^2 + |MB|^2}} dx_3 \quad (29)$$

$$\frac{1}{K_{s3}} = \int_0^{d_3} \frac{1.2\cos^2\left[\alpha_1 + \arctan(x_3/|MB|)\right]}{GW\sqrt{x_3^2 + |MB|^2}} dx_3 \quad (30)$$

of which

$$|MB| = R_g\sin\theta_f + \frac{R_g\sin\varphi - q\sin\nu - h_r}{R_a\cos\alpha_K - R_g\cos\theta_f + d_3}\left(R_a\cos\alpha_K - R_g\cos\theta_f + x_3\right) + h_r \quad (31)$$

Yang and Sun [42] proposed the contact stiffness calculation formula based on the Hertz contact theory, which is widely adopted by scholars in the calculation modelling of TVMS, such as [19-20, 31-32, 37, 39]. The Hertz contact stiffness K_h can be expressed as [42],

$$\frac{1}{K_h} = \frac{4(1-\nu^2)}{\pi EW} \quad (32)$$

The gear tooth fillet foundation stiffness is also an important part of the TVMS. Chen [32] modified the computational method in [43] to fulfil the fillet foundation stiffness computation for the cracked gear. However, Chen's method will produce a large error when calculating the tooth fillet foundation stiffness of body cracked gears and only performs well in the case of tooth crack. Therefore, Yang and Wang [30] further modified Chen's model and proposed a tooth fillet foundation stiffness calculation method for the cracked gears, which can meet the calculation for both the tooth and body cracked gears and can be expressed as [30],

$$\frac{1}{K_f} = \frac{\cos^2(\alpha_1 + \gamma)}{EW}\left[L\left(\frac{\mu_f'}{S_f'}\right)^2 + M\left(\frac{\mu_f'}{S_f'}\right) + P\left(1 + Q\tan^2(\alpha_1 + \gamma)\right)\right] \quad (33)$$

of which

$$S_f' = |BQ| = \sqrt{d_3^2 + (R_g\sin\varphi - q\sin\nu + R_g\sin\theta_f)^2} \quad (34)$$

$$\mu_f' = \left[\frac{1}{2}S_f' + \sqrt{\left(\frac{|GH| + |GB|\tan\gamma}{\tan\gamma + \tan\alpha_1} - |GB|\right)^2 + \left(\frac{-\tan\alpha_1(|GH| + |GB|\tan\gamma)}{\tan\gamma + \tan\alpha_1} + |GH|\right)^2}\right]\tan(\alpha_1 + \gamma) \quad (35)$$

Here,

$$\gamma = \angle A'BQ = \arcsin\left(d_3 / S_f'\right) \tag{36}$$

In Eq. (33), the calculation for parameters, L, M, P and Q can be found in Ref. [43].

Finally, the TVMS of single tooth pair can be calculated as,

$$K = \frac{1}{\left(\frac{1}{K_{bp}} + \frac{1}{K_{sp}} + \frac{1}{K_{ap}} + \frac{1}{K_{fp}} + \frac{1}{K_{bg}} + \frac{1}{K_{sg}} + \frac{1}{K_{ag}} + \frac{1}{K_{fg}} + \frac{1}{K_h}\right)} \tag{37}$$

of which, the subscripts p and g refer to the driving gear and driven gear respectively.

The existence of tooth profile errors and elastic deformation of the tooth may lead to gear failure to engage in accordance with the original meshing phase, which will further affect TVMS. Thus, the original TVMS calculation model needs to be further corrected by the tooth errors. The TVMS of single tooth pair is a function of tooth deformation δ_j (j denotes the numbering order of tooth pairs) and meshing position ϕ, which can be expressed as,

$$K_j = K_j\left(\phi, \delta_j\right) = \begin{cases} K_j(\phi), \delta_j > 0 \\ 0, \quad \delta_j \le 0 \end{cases} \tag{38}$$

Then, the total equivalent TVMS of double tooth pairs modified by the tooth errors can be deduced as [38],

$$k_m = \frac{\sum_{j=1}^{n} K_j}{1 + \sum_{j=1}^{n} K_j E_{kj} / F} \tag{39}$$

where, n=1, 2 refers to the first and second tooth pair respectively. E_{kj} refers to the relative profile error of the tooth pair j relative to the maximum deformation tooth pair k, and can be deduced as

$$E_{kj} = E_{pj} + E_{gj} - E_{pk} - E_{gk} \tag{40}$$

Here, subscript j refers to any tooth pair and subscript k represents the maximum deformation tooth pair. subscripts p and g denote the driving gear and driven gear respectively.

3. Parameter definition of tooth TR

Fig. 5 shows the definition of gear tooth TR parameters. In this paper, the same amount and same length of tooth TR are assumed for both the driving and driven gears, and the parabola is adopted as the tooth TR shape. The amount and length of tooth TR are given as follows [38]:

$$C_n = \frac{C_a}{C_{a\_\max}} \tag{41}$$

$$L_n = \frac{L_a}{L_{a\_\max}} \tag{42}$$

where $C_{a\_\max} = 0.02m$ and $L_{a\_\max} = 0.6m$ [38], in which m denotes the module of the gear.

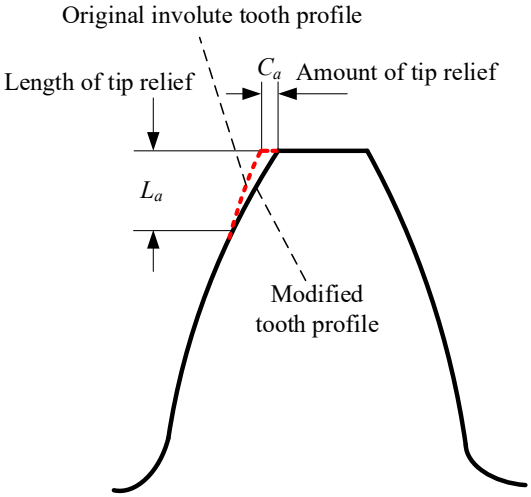

Fig. 5 Schematic of tooth TR

Based on the equations established above, the TVMS calculation flow chart of the proposed model is given and displayed in Fig. 6.

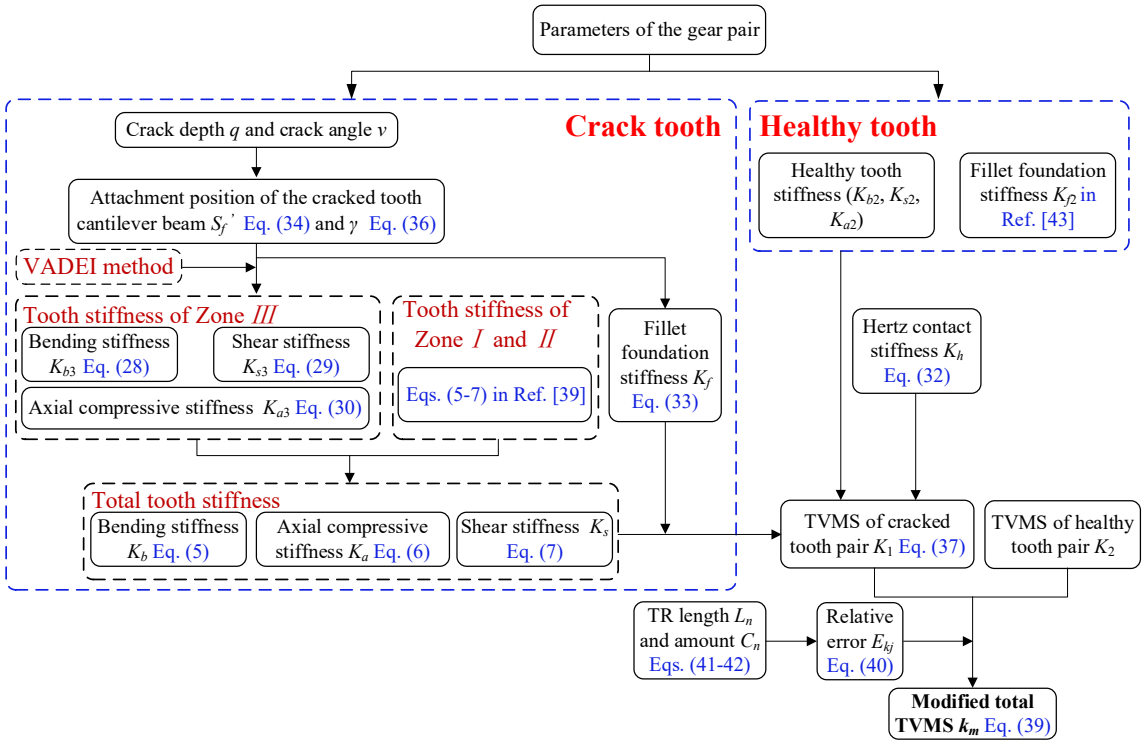

Fig. 6 Flow chart of the proposed TVMS calculation model

4. FE modelling for validating the proposed TVMS calculation model

Although the FE model has low computational efficiency, it is often used by scholars to validate the accuracy and correctness of the proposed analytical TVMS calculation model due to its high computational accuracy. At present, there are two kinds of FE models widely used to calculate the gear TVMS: the FE models by applying contact force [26, 30-32] and FE models with contact elements [13, 15, 31]. By contrast, the calculation efficiency of the FE models with contact elements is relatively lower, especially when a large number of grids are involved [31].

Therefore, to facilitate modelling and improve computational efficiency, the 2D FE models by applying contact force are adopted in this study.

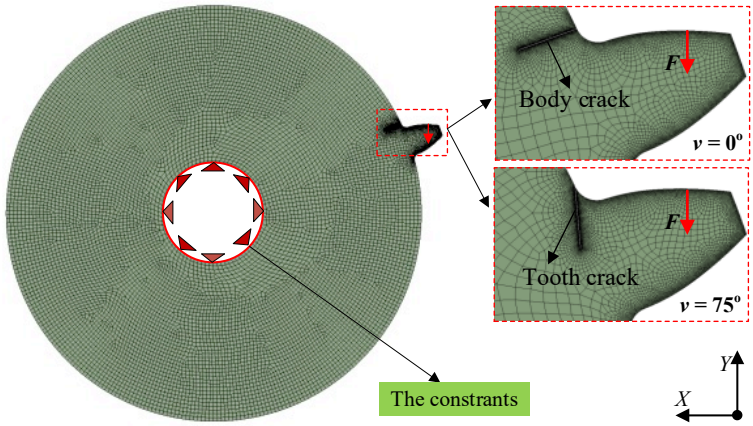

Fig. 7 FE models of spur gear with different types of cracks

The established 2D FE models of the cracked gear are presented in Fig. 7. To verify the universality of the proposed analytical model, two types of crack models were both established in this study, that is

1) Body crack models: The crack angle v = 0°, and the crack depth q = 0.5 mm, 1 mm, 1.5 mm and 2 mm, respectively. In this case, with the crack increase, the effective tooth thickness of the crack gear is almost unchanged, and the length of the tooth cantilever beam gradually increases.

2) Tooth crack models: The crack angle v = 75°, and the crack depth q = 0.5 mm, 1 mm, 1.5 mm and 2 mm, respectively. In this case, with the crack increasing, the effective tooth thickness changes greatly while the length of the tooth cantilever beam changes slightly.

Through computing the displacement of the meshing point of driving and driven gears along the line of action under meshing force F, the TVMS can be finally obtained by [26, 30, 32],

$$K_{fFEM} = \frac{F}{\delta_p + \delta_g} \tag{43}$$

where K_{fFEM} is the TVMS of the single tooth pair calculated by the FE model. δ_p and δ_g represent the meshing point displacement of driving and driven gears along the line of action, respectively.

5. Dynamic modelling of spur gear system

To study the fault vibration characteristics, and then provide the corresponding theoretical basis for the establishment of the crack fault diagnosis method, a lumped parameter dynamic model with 6-DOF is established and shown in Fig. 8. In the developed dynamic model, the internal excitation of transmission error and TVMS are all considered. Since the similar dynamics models of double tooth pairs have been verified and widely used, such as in Refs. [18, 26, 29], the correctness of the dynamic model is not repeatedly verified in this paper. It is worth noting that, different from the 6-DOF dynamics model in Refs. [26, 29], the proposed dynamic model takes into account the plane circumferential distribution position of the gear system, that is, the vibration response along the x or y direction under different distribution position angles can be calculated by changing the angle position α_p. In this study, α_p is set as 20°.

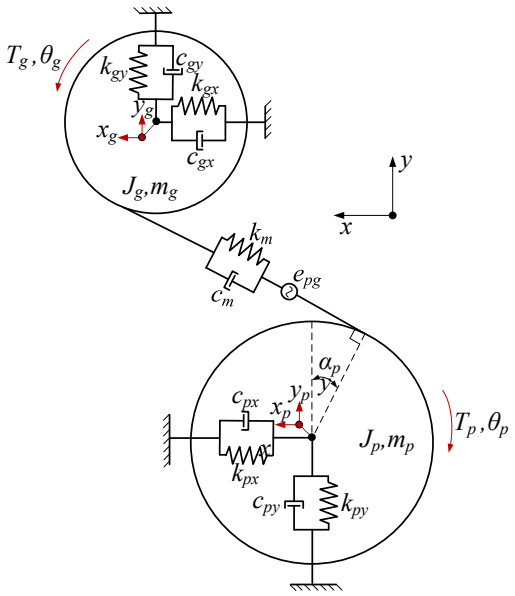

Fig. 8 The established dynamic model of the spur gear system

The vibration equation of the gear system can be given as,

$$\mathbf{M}\ddot{\mathbf{X}} + \mathbf{C}\dot{\mathbf{X}} + \mathbf{K}\mathbf{X} = \mathbf{P} \tag{44}$$

of which, the matrix of displacement **X,** mass **M**, damping **C**, stiffness **K** and load **P** can be deduced separately as follows,

$$\mathbf{X} = \left\lfloor x_p, y_p, \theta_p, x_g, y_g, \theta_g \right\rfloor \tag{45}$$

$$\mathbf{M} = \begin{bmatrix} m_p & & & & & \\ & m_p & & & & \\ & & J_p & & & \\ & & & m_g & & \\ & & & & m_g & \\ & & & & & J_g \end{bmatrix} \tag{46}$$

$$\mathbf{C} = \begin{bmatrix} c_{px}+c_m\cos^2\alpha_p & c_m\cos\alpha_p\sin\alpha_p & c_m\cos\alpha_p R_{bp} & -c_m\cos^2\alpha_p & -c_m\cos\alpha_p\sin\alpha_p & c_m\cos\alpha_p R_{bg} \\ c_m\cos\alpha_p\sin\alpha_p & c_{py}+c_m\sin^2\alpha_p & c_m\sin\alpha_p R_{bp} & -c_m\cos\alpha_p\sin\alpha_p & -c_m\sin^2\alpha_p & c_m\sin\alpha_p R_{bg} \\ c_m\cos\alpha_p R_{bp} & c_m\sin\alpha_p R_{bp} & c_m R^2{}_{bp} & -c_m\cos\alpha_p R_{bp} & -c_m\sin\alpha_p R_{bp} & c_m R_{bp} R_{bg} \\ -c_m\cos^2\alpha_p & -c_m\cos\alpha_p\sin\alpha_p & -c_m\cos\alpha_p R_{bp} & c_{gx}+c_m\cos^2\alpha_p & c_m\cos\alpha_p\sin\alpha_p & -c_m\cos\alpha_p R_{bg} \\ -c_m\cos\alpha_p\sin\alpha_p & -c_m\sin^2\alpha_p & -c_m\sin\alpha_p R_{bp} & c_m\cos\alpha_p\sin\alpha_p & c_{gy}+c_m\sin^2\alpha_p & -c_m\sin\alpha_p R_{bg} \\ c_m\cos\alpha_p R_{bg} & c_m\sin\alpha_p R_{bg} & c_m R_{bp} R_{bg} & -c_m\cos\alpha_p R_{bg} & -c_m\sin\alpha_p R_{bg} & c_m R^2{}_{bg} \end{bmatrix} \tag{47}$$

$$\mathbf{K} = \begin{bmatrix} k_{px}+k_m\cos^2\alpha_p & k_m\cos\alpha_p\sin\alpha_p & k_m\cos\alpha_p R_{bp} & -k_m\cos^2\alpha_p & -k_m\cos\alpha_p\sin\alpha_p & k_m\cos\alpha_p R_{bg} \\ k_m\cos\alpha_p\sin\alpha_p & k_{py}+k_m\sin^2\alpha_p & k_m\sin\alpha_p R_{bp} & -k_m\cos\alpha_p\sin\alpha_p & -k_m\sin^2\alpha_p & k_m\sin\alpha_p R_{bg} \\ k_m\cos\alpha_p R_{bp} & k_m\sin\alpha_p R_{bp} & k_m R^2{}_{bp} & -k_m\cos\alpha_p R_{bp} & -k_m\sin\alpha_p R_{bp} & k_m R_{bp} R_{bg} \\ -k_m\cos^2\alpha_p & -k_m\cos\alpha_p\sin\alpha_p & -k_m\cos\alpha_p R_{bp} & k_{gx}+k_m\cos^2\alpha_p & k_m\cos\alpha_p\sin\alpha_p & -k_m\cos\alpha_p R_{bg} \\ -k_m\cos\alpha_p\sin\alpha_p & -k_m\sin^2\alpha_p & -k_m\sin\alpha_p R_{bp} & k_m\cos\alpha_p\sin\alpha_p & k_{gy}+k_m\sin^2\alpha_p & -k_m\sin\alpha_p R_{bg} \\ k_m\cos\alpha_p R_{bg} & k_m\sin\alpha_p R_{bg} & k_m R_{bp} R_{bg} & -k_m\cos\alpha_p R_{bg} & -k_m\sin\alpha_p R_{bg} & k_m R^2{}_{bg} \end{bmatrix} \tag{48}$$

$$\mathbf{P}=\begin{bmatrix}\left(c_m\dot{e}_{pg}+k_m e_{pg}\right)\cos\alpha_p\\ \left(c_m\dot{e}_{pg}+k_m e_{pg}\right)\sin\alpha_p\\ \left(c_m\dot{e}_{pg}+k_m e_{pg}\right)R_{bp}+T_p\\ -\left(c_m\dot{e}_{pg}+k_m e_{pg}\right)\cos\alpha_p\\ -\left(c_m\dot{e}_{pg}+k_m e_{pg}\right)\sin\alpha_p\\ \left(c_m\dot{e}_{pg}+k_m e_{pg}\right)R_{bg}+T_g\end{bmatrix} \tag{49}$$

In Eqs. (45)-(49), the explanation of the symbols can be seen in the List of symbols.

By inputting the element parameters in the matrix of mass **M**, damping **C**, stiffness **K** and load **P** into Eq. (44), the displacement responses **X** can be obtained through solving Eq. (44) using the Runge-Kutta method in Matlab, and then the vibration responses of the gear system can be further analyzed.

6. Results and discussion

Based on the TVMS calculation models and 6-DOF dynamic model established in the previous sections, the characteristics of the TVMS excitation and dynamic responses of the gear system are calculated and analyzed in this section. The parameters of the gear system used in this simulation study are displayed in Table 1.

Table 1 Design parameters of spur gear system used in the simulation

Parameter	Driving gear	Driven gear
Teeth number n	30	25
Modulus m (mm)	2	2
Tooth width W (mm)	20	20
Contact ratio	1.63	1.63
Pressure angle α_0 (°)	20	20
Poisson's ratio	0.3	0.3
Young modulus E (GPa)	206.8	206.8
Mass (kg)	m_p=0.4439	m_g=0.3083
Rotational inertia (kg·m^2)	J_p=2×10^{-4}	J_g=0.96×10^{-4}
Radial bearing stiffness (N/m)	k_{px}=k_{py}=6.56×10^8	k_{gx}=k_{gy}=6.56×10^8
Radial bearing damping (N·s/m)	c_{px}=c_{py}=1.8×10^3	c_{gx}=c_{gy}=1.8×10^3
Rotational speed (rpm)	ω_p=2000	ω_g=2400
Mesh damping between meshing teeth c_m (N·s/m)	0.3e-5×k_m [41]	

6.1 Analysis of TVMS calculation results

In this section, the correctness and accuracy of the proposed analytical TVMS calculation model of cracked gear are validated by the FE method. Then, the effects of parameters of load, TR and crack on the TVMS are analyzed and discussed based on the proposed model.

6.1.1 Verification results of the proposed TVMS calculation model

Fig. 9 shows the comparison of TVMS results calculated by the proposed model, traditional model and FE model under different depths with the same crack angle v = 0°. In this comparative

study, the tooth profile of gear is not modified.

As can be seen in Fig. 9, the TVMS calculated by the proposed model and the FE model gradually decreases and are in good agreement with each other as the crack increases, while the traditional model almost keeps a constant value. The results indicate that the lengthening of the tooth cantilever beam caused by the body crack will weaken the tooth stiffness, and the deeper the crack is, the greater the weakening effect will be. Since the crack angle v = 0°, the effective thickness of the cracked tooth is barely affected by the crack propagation, thus the TVMS obtained from the traditional model is almost a constant value with the increase of the crack depth, which is not in line with the actual situation. In conclusion, the good agreement between the proposed model and the FE model verifies the correctness and accuracy of the proposed model.

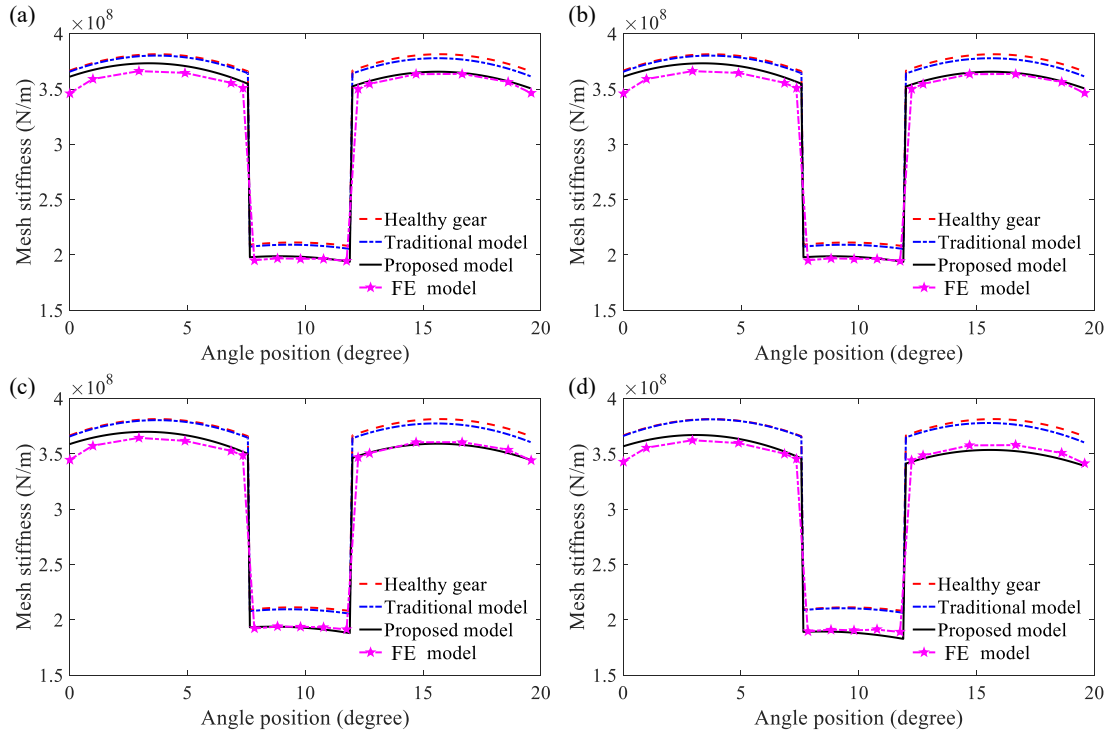

Fig. 9 TVMS comparison of body cracked gear (v = 0°) obtained from different models under different crack depths: (a) q = 0.5 mm, (b) q = 1 mm, (c) q = 1.5 mm, (d) q = 2 mm

To verify that the proposed model also has high calculation accuracy in the tooth crack case, the comparison of TVMS results obtained from the three models under different tooth crack depths is also carried out in Fig. 10. It can be seen that the TVMS calculated by the three models decrease with the raising of the tooth crack depth and are all in good agreement, indicating that the proposed model can also be used in tooth crack cases.

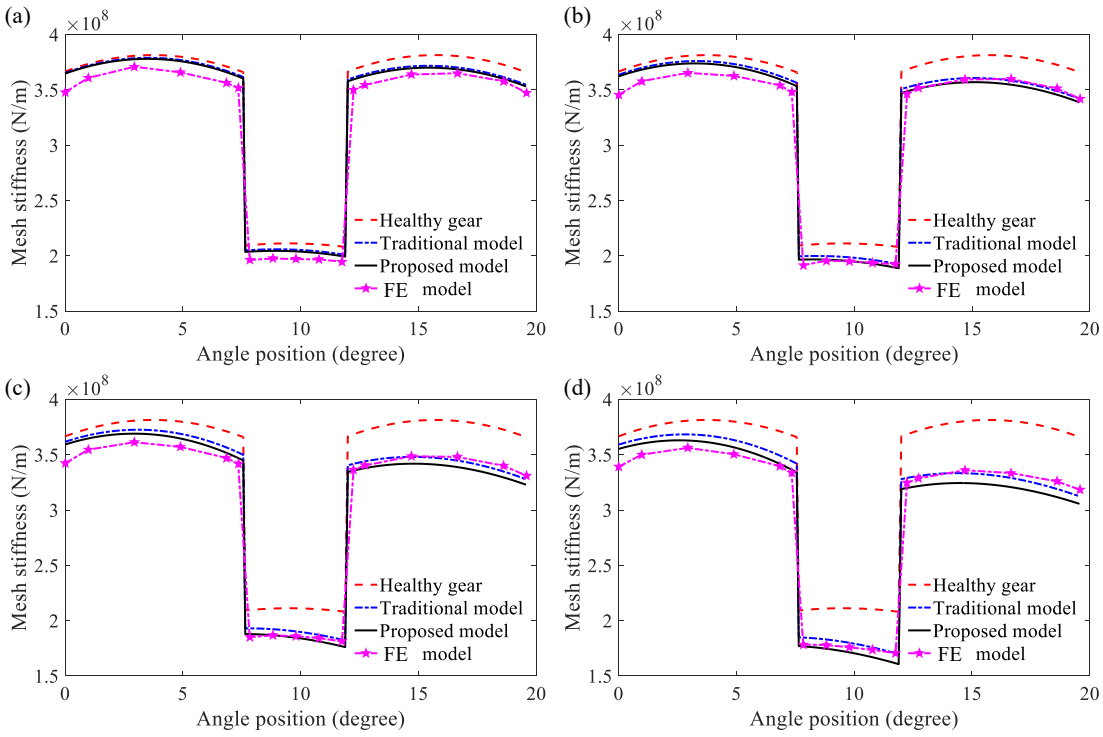

Fig. 10 TVMS comparison of tooth crack gear (v = 75°) obtained from different models under different crack depths: (a) q = 0.5 mm, (b) q = 1 mm, (c) q = 1.5 mm, (d) q = 2 mm

To further clearly present the comparison results, the percentage differences of the TVMS results computed by the proposed and traditional models from the FE model under different crack cases are displayed in Table 2. As can be found, for the body crack case (v = 0°), the percentage differences of the traditional model are significantly larger than that of the proposed model, especially when the crack becomes larger. For example, the percentage difference of the traditional model is up to about 25.6 times that of the proposed model under the case q = 2 mm. For the tooth crack case (v = 75°), the percentage differences between the traditional and proposed models are close to each other, but the proposed model is relatively smaller, which demonstrates that the slight tooth lengthening induced by the crack with v = 75° also affects on TVMS.

Table 2 Percentage differences of the TVMS calculated by proposed and traditional models from the FE model

Crack parameters		Percentage difference (%)	
Crack angle v (°)	Crack depth q (mm)	Traditional model	Proposed model
0	0.5	3.92	2.22
	1	4.68	1.21
	1.5	5.73	0.42
	2	6.91	0.27
75	0.5	3.06	2.58
	1	1.84	0.76
	1.5	1.93	0.03
	2	1.70	1.24

From the above validation results, we can conclude that the main advantage of the proposed model is its high calculation accuracy in the body crack case, which is not possible with the traditional model. However, in the case of the tooth crack, the differences between the proposed and traditional models are relatively small because the attachment position of the cracked tooth in the proposed model is close to that of the traditional model. Therefore, both models can be used for TVMS calculation in the tooth crack case, while in the case of body crack, the proposed model

with higher accuracy is recommended.

6.1.2 Effects of TR parameters on TVMS of cracked gear

The TVMS results calculated by the proposed model under different amounts and lengths of TR are carried out to explore the effects of TR on the TVMS excitation of the cracked gear.

Fig. 11 displays the TVMS results of the body and tooth cracked gears with different TR amounts. It can be found in the unmodified case $C_n = 0$, there will be a sudden change of TVMS in the alternating region between the double-tooth meshing zone (DTMZ) and single-tooth meshing zone (STMZ), where the original DTMZ and STMZ are marked in Fig. 11. Compared with the unmodified gear, the gear with TR can slow down the sharp change of TVMS in the alternating region, which will reduce the TVMS excitation of the cracked gear. It can also be seen that compared to the original STMZ of the unmodified case, the STMZ of the modified cracked gear increases gradually with the TR amount rising (This change is denoted in Fig. 11 (a) using case C_n = 1.5 as an example), which is because the error caused by the TR delays the time of the double teeth into the engagement. Moreover, the corner contact will be easy to occur when the TR amount is relatively small, such as the part marked by the ellipse in the case $C_n = 0.3$. By comparing case $C_n = 0.6$ in Fig. 11 (a) and (b), it can be observed that the engaged position of the second DTMZ (As indicated by the abscissa of the black dot) of the body cracked tooth is 0.01 mesh cycles later than that of the tooth crack tooth, which indicates that the tooth cracked tooth is more likely to lead to the next tooth pair in advance into meshing and then cause corner contact phenomenon than the body cracked one under the same TR amount. This phenomenon is caused by the fact that the deformation of the tooth cracked gear is larger than that of the body cracked one under the same crack depth, which makes it easier to get the next tooth pair into engagement earlier.

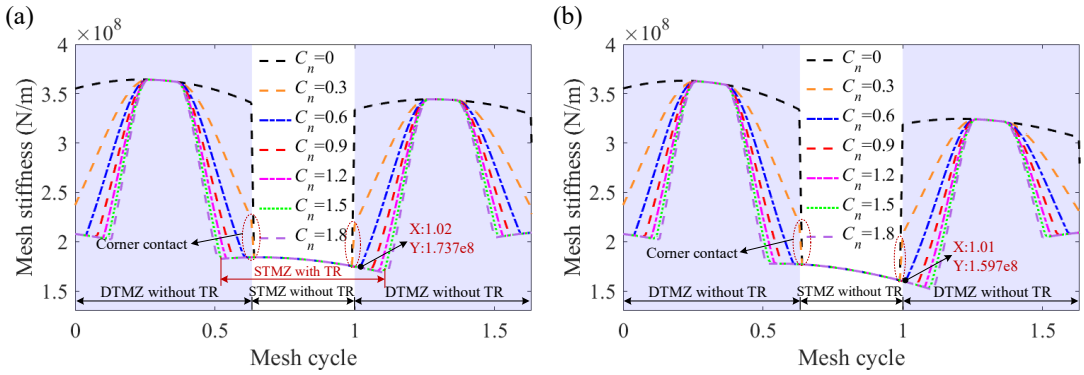

Fig. 11 Effects of TR amount C_n on TVMS under different crack types (q = 2 mm, T_p = 100 N and L_n = 0.6): (a) body crack (v = 15°), (b) tooth crack (v = 75°)

Fig. 12 presents the TVMS results of the body and tooth cracked gears with different TR lengths. We can see that the STMZ of both the body and tooth cracked gears increases with the TR length raising. The TVMS curve becomes smoother with L_n increasing when L_n is less than 0.8. However, the TVMS curve will become sharper and the bearing capacity of the cracked tooth will be significantly reduced when L_n = 0.8, 1.0 and 1.2. The tooth cracked tooth is more likely to lead to the corner contact phenomenon than the body cracked one under the same TR length, which can be found by comparing the abscissa of the black dot in case $L_n = 0.4$ in Fig. 12 (a) and (b). It can be concluded that tooth modification can change the phase and amplitude of the TVMS excitation of the cracked gear. Although the tooth modification can reduce the internal TVMS excitation, the

parameters of tooth TR amount and length should be selected reasonably according to the specific situation [38].

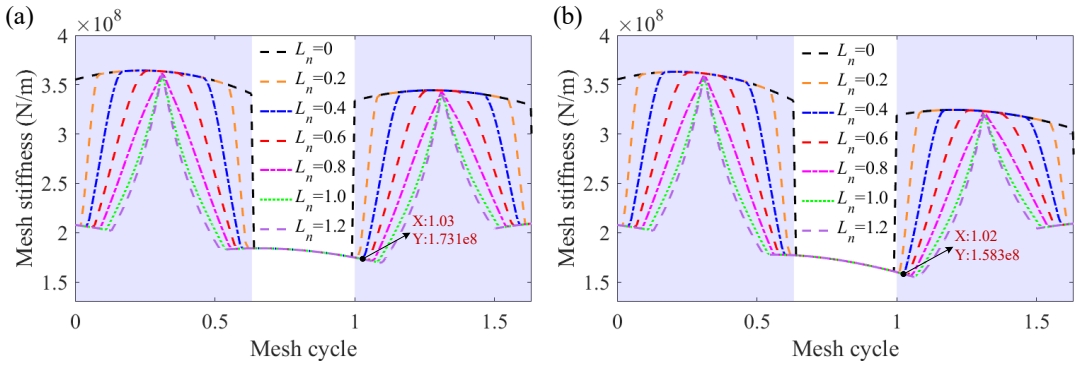

Fig. 12 Effects of TR length L_n on TVMS under different crack types (q = 2 mm, T_p = 100 N and C_n = 0.8): (a) body crack (v = 15°), (b) tooth crack (v = 75°)

6.1.3 Effects of load parameters on TVMS of cracked gear

Fig. 13 shows the influences of applied load on the TVMS of cracked gears. We can see that the STMZ of cracked gear goes up gradually with the decrease of the load, which indicates that the phase of the internal excitation of the crack gear can also be changed by the load. And the increase of load will lead to the corner contact, such as the part marked by the ellipse in the case T_p = 200 N·m. Compared with the body crack case, the tooth cracked gear with the same crack depth is more prone to corner contact under the same load, which can be inferred by comparing the abscissa of the black dot in case T_p = 100 N·m. Similar to the previous results, this phenomenon is also because the TVMS of tooth cracked gear is smaller than the body cracked one, which makes it easier to get the next tooth pair into engagement earlier.

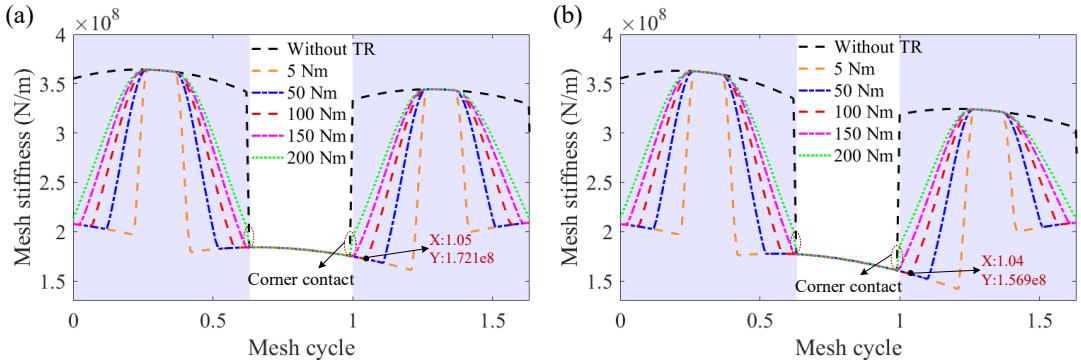

Fig. 13 Effects of load on TVMS under different crack types (q = 2 mm, C_n = 0.8 and L_n = 0.6): (a) body crack (v = 15°), (b) tooth crack (v = 75°)

6.1.4 Effects of crack parameters on TVMS

Fig. 14 displays the effects of crack depth on TVMS of the cracked gears. It can be observed that the TVMS of both the body and tooth cracked gears gradually rises with the increase of the crack depth. However, under the same crack depth, the TVMS of tooth cracked gear decreases more sharply than the body cracked one, which illustrates that the same value of effective tooth

thickness reduction has a more significant effect on the TVMS than the same value of tooth lengthening caused by the crack. In addition, the corner contact also occurs in the tooth cracked gear with crack depth q = 4 mm due to its relatively low TVMS.

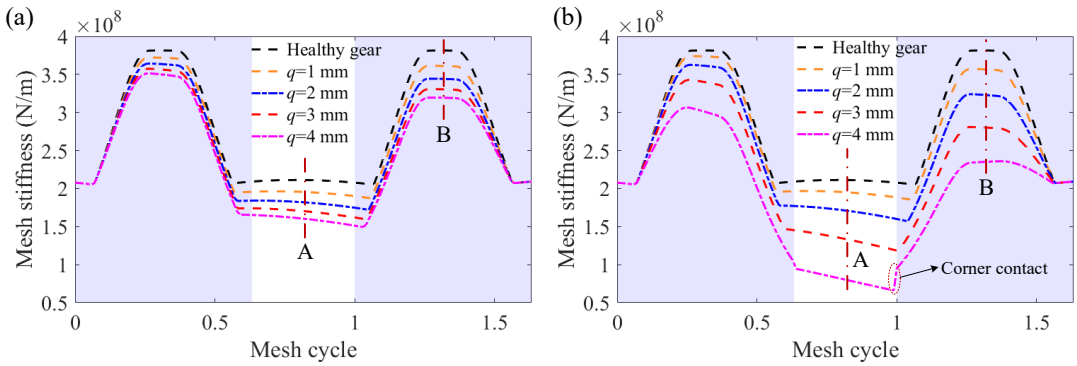

Fig. 14 Effects of crack depth on TVMS (T_p = 100 N, C_n = 0.8 and L_n = 0.6): (a) body crack (v = 15°), (b) tooth crack (v = 75°)

To quantify the weakening effect of different crack parameters on TVMS of cracked gears, the percentage differences of TVMS (P_{TVMS}) of cracked gears from healthy gear are carried out, which is defined as,

$$P_{TVMS} = \frac{TVMS_{Crack} - TVMS_{Healthy}}{TVMS_{Healthy}} \times 100\% \tag{50}$$

where, $TVMS_{Crack}$ and $TVMS_{Healthy}$ denote the TVMS of cracked and healthy gears at the same meshing position, respectively.

In Fig. 14, moments A and B represent the meshing position in STMZ and DTMZ, respectively. To clearly present the effects of crack parameters on the TVMS, the P_{TVMS} of different crack depth cases at moments A and B is calculated and displayed in Table 3. It can be seen that the same crack depth has different weakening effects on TVMS under different crack angles, especially in the larger crack depth case. For example, under the case q = 4 mm, the P_{TVMS} of the tooth cracked gear (v = 75°) can be respectively up to about -61% and -38.45% at moments A and B, while the body cracked case (v = 15°) only reaches -23.61% and -16.25% accordingly.

Table 3 P_{TVMS} of the cracked gear from the healthy gear under different crack depths

Crack angle v (°)	Crack depth q (mm)	Moment A		Moment B	
		TVMS (×10^8 N/m)	P_{TVMS} (%)	TVMS (×10^8 N/m)	P_{TVMS} (%)
15	0	2.113	0	3.815	0
	1	1.959	-7.26	3.612	-5.32
	2	1.826	-13.57	3.443	-9.76
	3	1.712	-18.97	3.305	-13.35
	4	1.614	-23.61	3.195	-16.25
75	1	1.957	-7.34	3.568	-6.48
	2	1.723	-18.43	3.234	-15.23
	3	1.356	-35.80	2.804	-26.49
	4	0.824	-61.00	2.348	-38.45

The influences of crack angles on the TVMS of cracked gears are shown in Fig. 15. It can be found in Fig. 15 (a) that the TVMS first decreases and then increases with the raising of the crack

angle, and the TVMS reaches the minimum at v = 45°. The results can be explained that the TVMS of cracked gear is co-determined by the following three factors: the effective tooth thickness and length, as well as the fillet foundation stiffness, which is all determined by the crack position. In this case, the comprehensive weakening effect of the three factors on TVMS reaches the maximum at 45°. From the whole view, the crack angle under the crack depth q = 1 mm has little influence on TVMS, mainly because the effect of the small size crack on the tooth attachment position is limited. In Fig. 15 (b), the TVMS decreases with the rising of the crack angle when q = 4 mm. This phenomenon is due to that in the large crack case, the change in effective tooth thickness has a more obvious impact on TVMS.

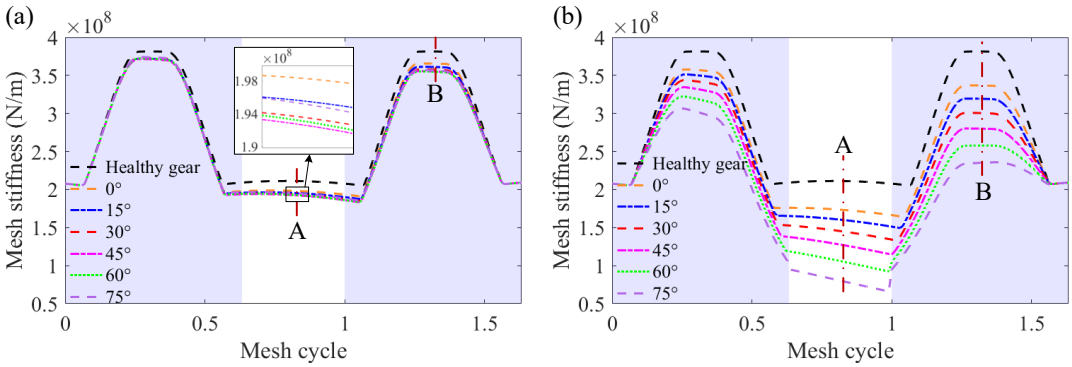

Fig. 15 Effects of crack angle on TVMS (T_p = 100 N, C_n = 0.8 and L_n = 0.6): (a) q = 1 mm, (b) q = 4 mm

Table 4 presents the P_{TVMS} of different crack angle cases at moments A and B. From Tables 3 and 4, it can be observed that with the crack angle rises, the PT_{TVMS} of moments A and B under the crack case q = 1 mm rarely changes, while it increases significantly under the crack case q = 4 mm. For example, when the crack angle increases from 0° to 75°, the maximum reduction of P_{TVMS} at moments A and B reaches -2.58% and -2.78% respectively in the crack case q = 1 mm, while this value is up to -43.43% and -26.75% accordingly in the case q = 4 mm. Therefore, it can be concluded that the TVMS is less affected by the crack angle under the small crack depth, but it is very sensitive to the crack angle under the large crack case.

Table 4 P_{TVMS} of the cracked gear from the healthy gear under different crack angles

Crack depth q (mm)	Crack angle v (°)	Moment A		Moment B	
		TVMS ($\times 10^8$ N/m)	P_{TVMS} (%)	TVMS ($\times 10^8$ N/m)	P_{TVMS} (%)
1	0	1.986	-6.00	3.657	-4.15
	30	1.940	-8.17	3.577	-6.24
	45	1.931	-8.58	3.555	-6.82
	60	1.936	-8.34	3.550	-6.93
4	0	1.741	-17.57	3.369	-11.70
	30	1.467	-30.56	3.007	-21.19
	45	1.293	-38.80	2.801	-26.57
	60	1.080	-48.90	2.578	-32.42

6.2 Analysis of dynamic simulation results

In this section, based on the 6-DOF dynamic model established in Section 5, the effects of different TVMS calculation models, TR, load and crack propagation on the vibration

characteristics of the tooth and body cracked gear are analyzed and discussed. The vibration signals of the driving gear in the *x*-direction are adopted in the following analysis.

6.2.1 Effects of different TVMS calculation models on the dynamic characteristics of cracked gear

To reveal the dynamic characteristic deviations caused by the traditional and proposed TVMS calculation models under tooth and body crack cases, the time and frequency domain spectra of the tooth and body cracked gear are carried out and presented in Fig. 16.

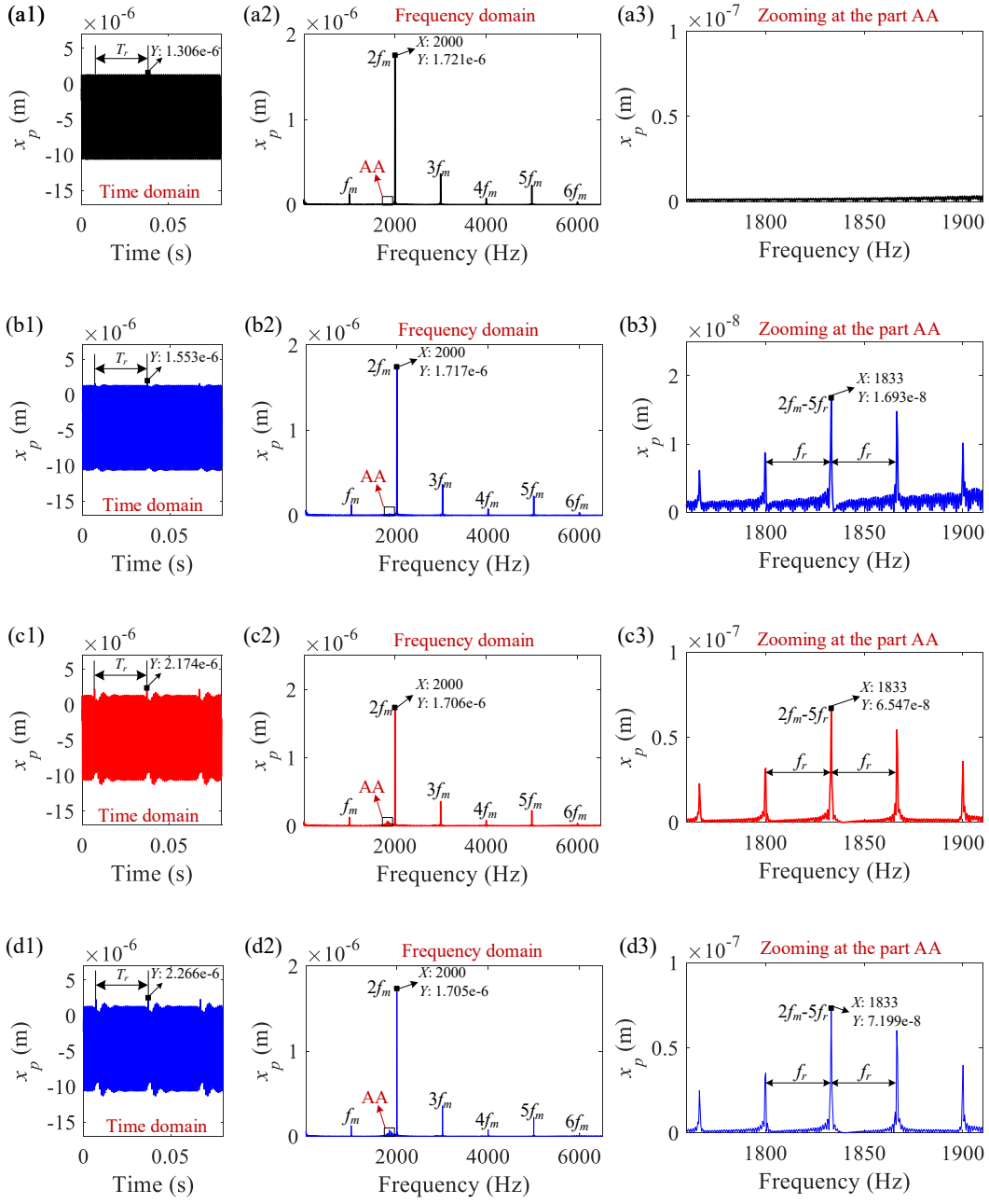

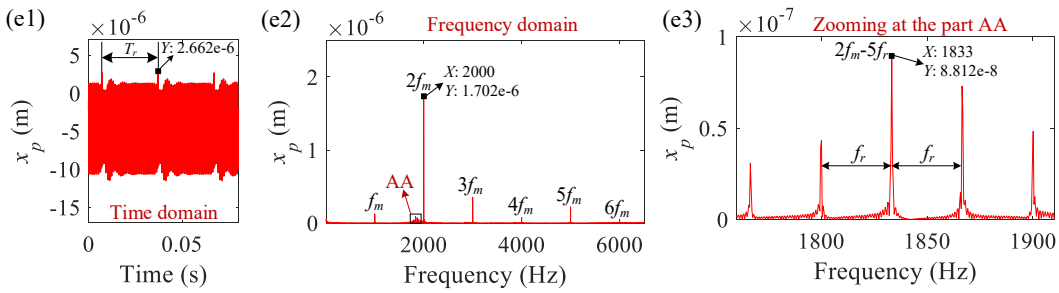

Fig. 16 Time and frequency domain spectra under different TVMS models and crack types (q = 2 mm, T_p = 100 N, C_n = 0.8 and L_n = 0.6): (a) healthy gear, (b) TM with BC, (c) PM with BC, (d) TM with TC, (e) PM with TC. (BC: Body crack (v = 15°); TC: Tooth crack (v = 75°); TM: Traditional model; PM: Proposed model)

It can be found in Fig. 16 that the crack will produce the periodic impact (presented in Fig.16 (b1), (c1), (d1) and (e1)) with the rotation cycle time T_r = 0.03 s in the time domain, which is caused by the periodic TVMS excitation of the crack tooth. Moreover, the crack can also lead to the frequency sidebands with an interval of the rotation frequency f_r (f_r = 33.33 Hz) near the meshing frequency f_m and its harmonic frequencies ($2f_m$, $3f_m$, …), which can be seen in Fig.16 (b2), (c2), (d2) and (e2). In the frequency spectrum, the main response frequency is $2f_m$, and the sideband near $2f_m$ is the most abundant. Therefore, the maximum amplitude of the side frequencies (MASF) near $2f_m$ is adopted to quantify the effects of the crack on the gear's vibration frequency domain spectra.

By comparing Fig. 16 (b1) with (c1) and Fig. 16 (d1) with (e1), we can see that the maximum amplitude of the periodic impact in the time spectra obtained by the traditional model in the body and tooth crack cases is about 1.553 μm and 2.266 μm respectively, while for the proposed model it reaches 2.174 μm and 2.662 μm accordingly. By comparing the frequency spectra, the MASF near $2f_m$ in Fig. 16 (c3) and (e3) is about 3.87 times and 1.22 times higher than that in Fig. 16 (b3) and (d3) respectively. From the above comparison, we can conclude that the time-domain response impact calculated based on the proposed model is larger than that of the traditional model. The deviations demonstrate that the weakening effect of tooth lengthening caused by the crack on the TVMS has a great influence on the vibration characteristics of crack fault, which can not be ignored.

From Fig. 16 (c) and (e) it can be observed that the periodic impact caused by the tooth crack is more intense than the body crack under the same crack depth. And the percentage differences of maximum amplitude of the periodic impact in the time domain caused by the tooth crack is about 1.56 times larger than the body crack case. In the frequency domain, the MASF near $2f_m$ in the tooth crack case (marked in Fig. 16 (e3)) is 1.35 times larger than the body cracks one (pictured in Fig. 16 (c3)). The results illustrate that the reduction of effective tooth thickness aroused by the tooth crack has a greater weakening effect on the dynamic response than the tooth lengthening caused by the body crack under the same crack depth.

6.2.2 Effects of TR on dynamic characteristics of cracked gear

From Section 6.1.2 we can see that the TR has a great influence on the internal excitation of the cracked gear, which may further affect the vibration characteristic of crack fault. Therefore, the effects of TR on the dynamic characteristics of cracked gear are carried out and displayed in Fig.17. It can be found in Fig. 17 (a) that the TR will reduce the vibration levels of the cracked

gear, but it doesn't mean that the larger the TR amount, the more the vibration decreases. Therefore, it is very important to select appropriate tooth modification parameters. From Fig. 17 (b) we can find that as the TR amount increases, the peak position of the sideband gradually moves away from $2f_m$ (that is, from $2f_m$-$2f_r$ to $2f_m$-$5f_r$), and its amplitude decreases gradually. These differences are due to the fact that the TR changes the amplitude and alternating position between the DTMZ and STMZ of the TVMS internal excitation, which leads to different behaviors of phase and amplitude modulations caused by the periodic impact of crack fault.

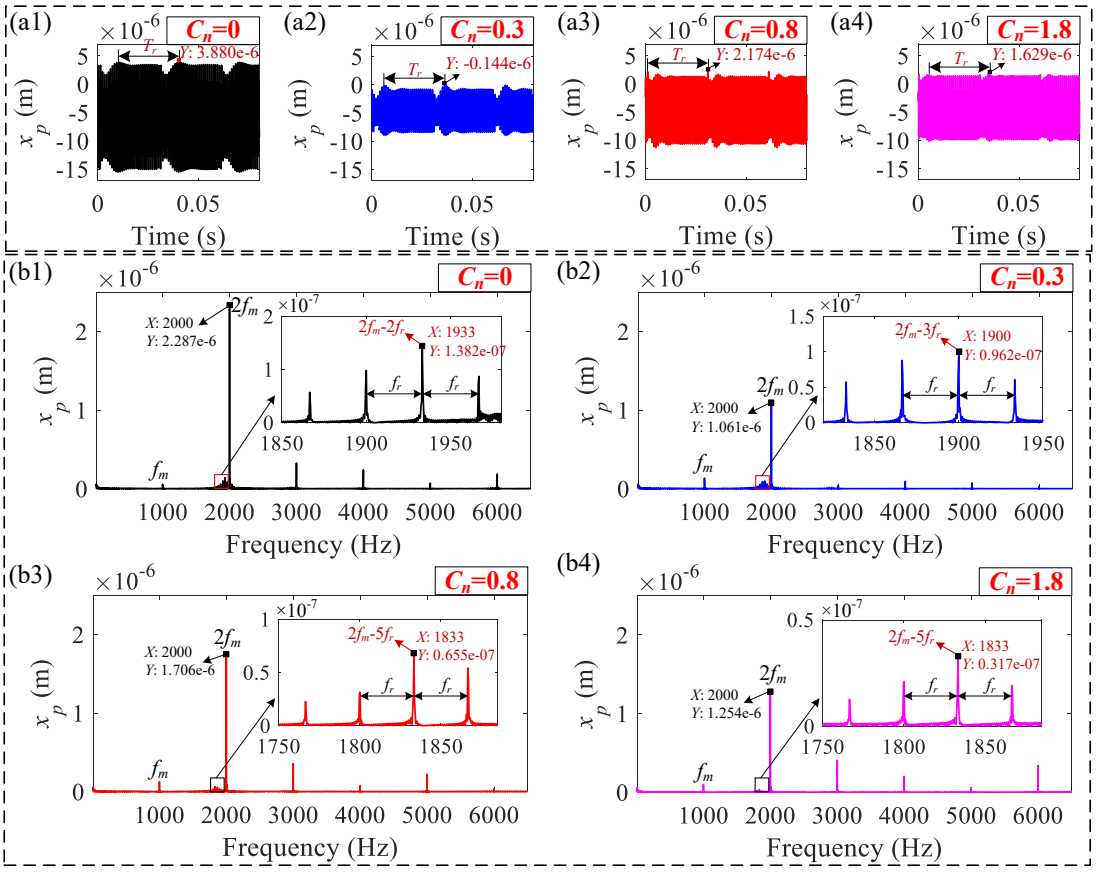

Fig. 17 Time and frequency domain spectra of cracked gear with different TR amounts C_n (v = 15°, q = 2 mm, T_p = 100 N and L_n = 0.6): (a) time domain, (b) frequency domain

Scholars usually use the ratio of amplitude between the side frequency and meshing frequency to characterize the degree of crack failures [44]. In our study, two frequency domain indicators are put forward to clearly present the differences in frequency domain characteristics of the cracked gear under different cases, which are expressed by,

$$R_{MASF} = \frac{\mathrm{Max}(A_{nf_m \pm if_r})}{A_{nf_m}} \times 100\% \tag{51}$$

$$R_{SASF} = \frac{\sum_{i=1}^{k} A_{nf_m \pm if_r}}{A_{nf_m}} \times 100\% \tag{52}$$

where R_{MASF} and R_{SASF} represent the ratio of the MASF and the sum of amplitudes of side frequencies (SASF) to the amplitude of the meshing frequency, respectively. $A_{nfm\pm ifr}$ means the

amplitude of the ith side frequency on both sides of the nth meshing frequency, A_{nfm} is the amplitude of the nth meshing frequency, and k denotes the number of side frequencies. In this study, $k = 29$ and $n = 2$.

Fig. 18 displays the effects of TR amount on the spectrum characteristic parameters of the cracked gear. It can be found in Fig. 18 (a) that the amplitude of $2f_m$ reaches the minimum at $C_n = 0.3$, which reflects that the vibration of the cracked gear is greatly reduced in this case. In Fig. 18 (b), with the TR amount going up, the amplitude of MASF and SASF decreases gradually, and the peak position of the sideband gradually moves away from $2f_m$-$2f_r$ to $2f_m$-$5f_r$. In Fig. 18 (c), the R_{MASF} and R_{SASF} first increase and then decrease with the TR amount increasing, and both reach the maximum at $C_n = 0.3$, which indicates that the TR amount has a great influence on the spectrum statistical characteristic of the crack fault.

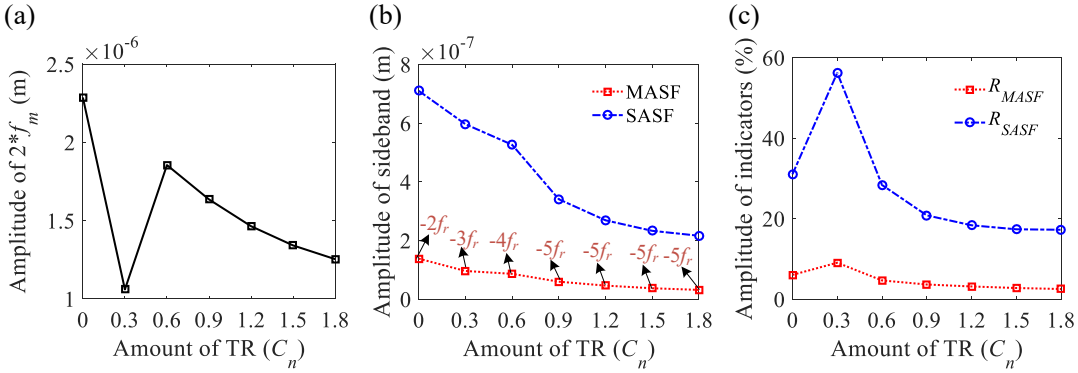

Fig. 18 Effects of TR amount C_n on frequency spectrum characteristic parameters of cracked gear ($\nu = 15°$, $q = 2$ mm, $T_p = 100$ N and $L_n = 0.6$): (a) meshing frequency, (b) side frequency, (c) frequency domain indicators

Fig. 19 presents the effects of TR length on the dynamic characteristics of the cracked gear. We can find that the relationship between TR length and the vibration amplitude of the cracked gear is also nonlinear, that is, the vibration amplitude does not decrease continuously with the increase of the TR length. The TR length also has a great effect on the dynamic characteristics of the cracked gear. Under the case of $L_n = 0.2$, the gear vibration level reaches the lowest, and the side frequency components near $2f_m$ are still abundant, but the amplitude of $2f_m$ decreases sharply compared with the other cases.

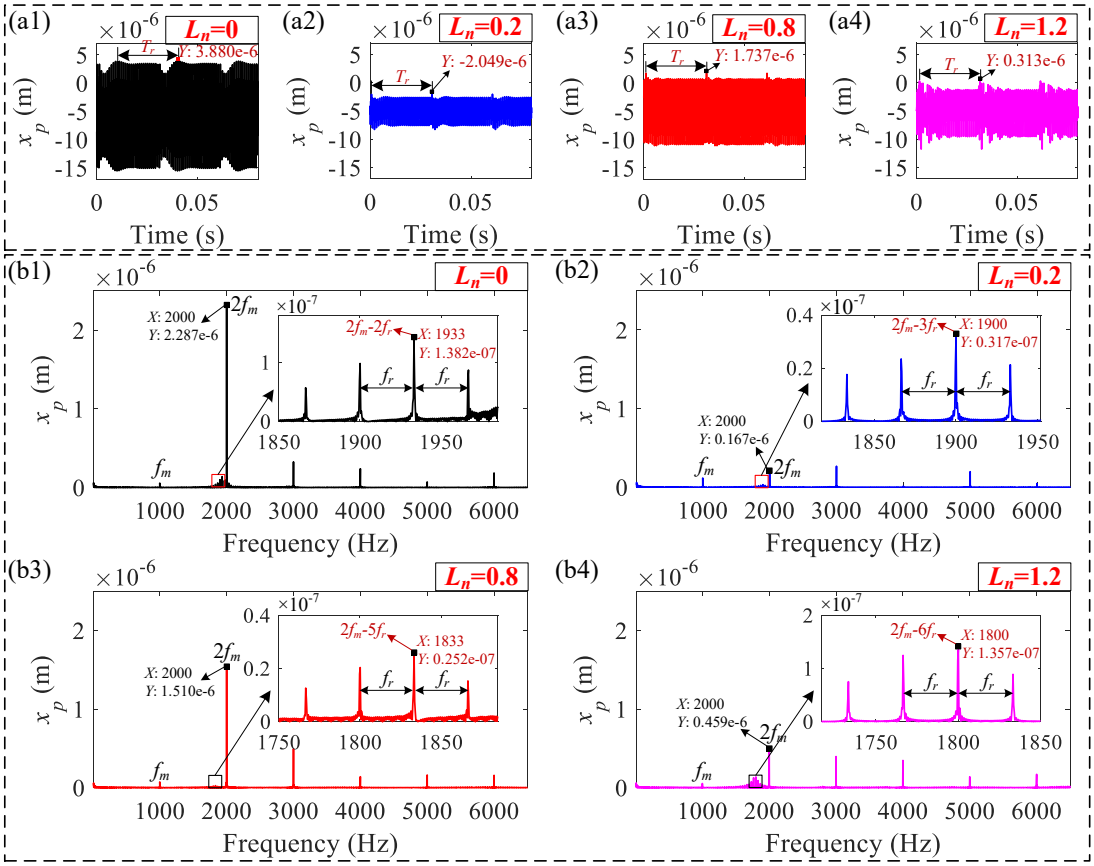

Fig. 19 Time and frequency domain spectra of cracked gear with different TR lengths L_n (ν = 15°, q = 2 mm, T_p = 100 N and C_n = 0.8): (a) time domain, (b) frequency domain

The effects of TR length on the spectrum characteristic parameters of cracked gear are also put forward in Fig. 20. It can be seen that the amplitude of $2f_m$ reaches the minimum at L_n = 0.2. Different from the effects of TR amount, the amplitudes of MASF and SASF do not decrease continuously with the increase of the TR length, but show a fluctuating state and reach the minimum at case L_n = 0.8. With the L_n increase, the peak position of the sideband gradually changes from $2f_m$-$2f_r$ to $2f_m$-$6f_r$. The amplitude of R_{MASF} and R_{SASF} is more obvious when L_n = 0.2 and 1.2.

The above results show that the vibration characteristics of cracked gears with different TR parameters are different under the same crack fault degree, and thus the influence of TR should be considered in the design of the crack fault diagnosis method.

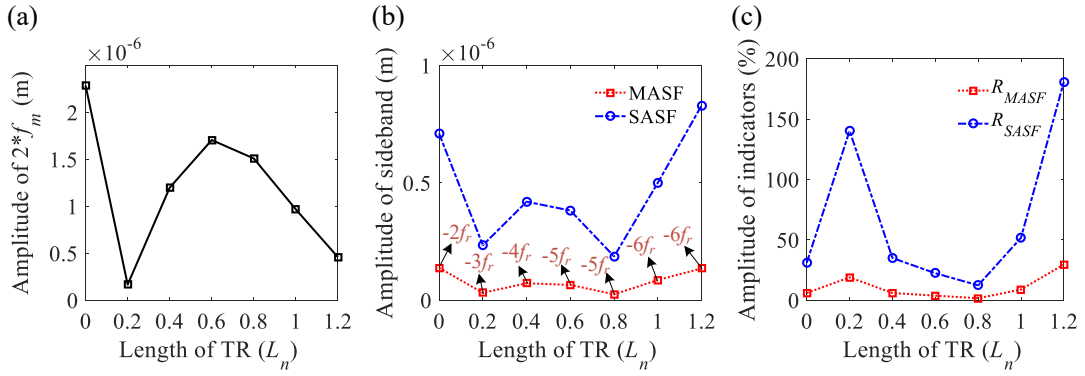

Fig. 20 Effects of TR length L_n on frequency spectrum characteristic parameters of cracked gear (v = 15°, q = 2 mm, T_p = 100 N and C_n = 0.8): (a) meshing frequency, (b) side frequency, (c) frequency domain indicators

6.2.3 Effects of load on dynamic characteristics of cracked gear

The effects of load on the dynamic characteristics of the cracked gear are also studied and displayed in Fig. 21. It can be seen that with the load rising, the vibration of the cracked gear increases, and the amplitudes of the side frequencies and the meshing frequency $2f_m$ also rise gradually, which demonstrates that the load also has an important effect on the fault vibration characteristics of the cracked gear.

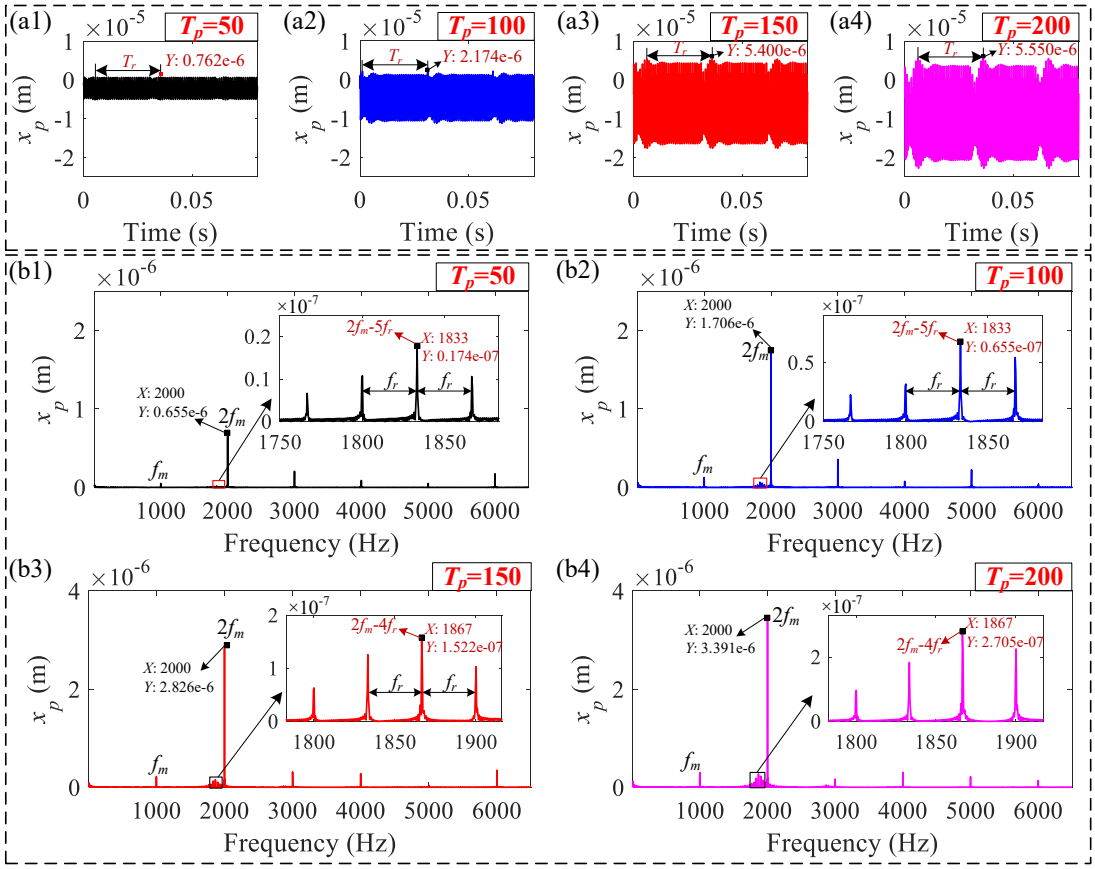

Fig. 21 Time and frequency domain spectra of cracked gear with different loads T_p (v = 15°, q= 2 mm, C_n = 0.8 and L_n = 0.6): (a) time domain, (b) frequency domain

The effects of load on the spectrum characteristic parameters of the cracked gear can be found in Fig. 22. It can be observed that with the load going up, the MASF, SASF and the amplitude of $2f_m$ all increase, and the peak position of the sideband gradually changes from $2f_m$-$7f_r$ to $2f_m$-$4f_r$, which demonstrates that the load can significantly influence the phase and amplitude modulations caused by the periodic impact of crack fault. This phenomenon can be explained that the load can significantly change the phase and amplitude of the TVMS excitation of cracked gear with tooth errors, which can be seen in Fig. 13. The R_{MASF} and R_{SASF} tend to go up with the load increase, which indicates that the crack fault characteristics are more obvious and easier to be measured and obtained under the larger load conditions.

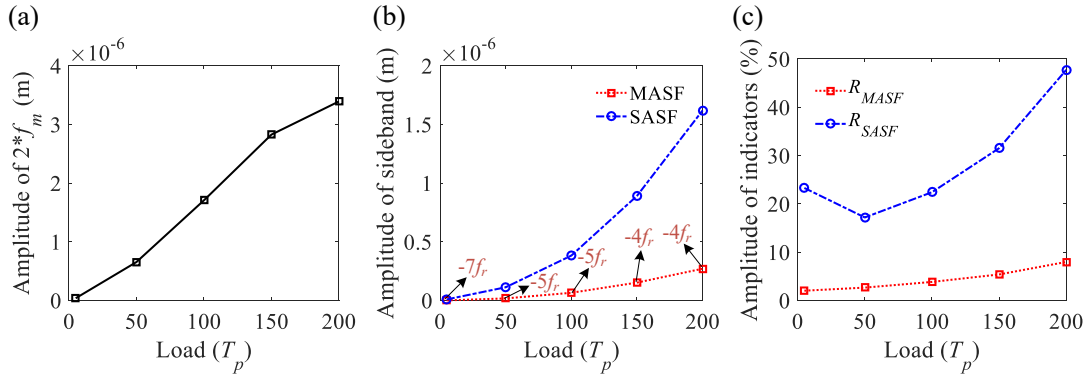

Fig. 22 Effects of load T_p on frequency spectrum characteristic parameters of cracked gear (ν = 15°, q= 2 mm, C_n = 0.8 and L_n = 0.6): (a) meshing frequency, (b) side frequency, (c) frequency domain indicators

6.2.4 Effects of crack propagation on dynamic characteristics of cracked gear

The study of the influence of crack propagation on gear dynamic responses can provide a theoretical basis for the method establishment of diagnosis and condition monitoring of crack failures. In this study, the influence of the body and tooth crack propagation on the dynamic characteristics of the gear system is carried out. And the crack propagation path is assumed to be a straight line, which is widely adopted by scholars [27-28, 39].

The time and frequency domain spectra under different body crack depths are displayed in Fig. 23. It can be found that the amplitude of the periodic impact in the time domain caused by the crack becomes larger with the crack propagating, which is mainly owing to the weakening effects of the tooth lengthening caused by the body crack on the TVMS increase with the crack propagation. In the frequency domain, with the body crack propagating, the MASF near $2f_m$ goes up, while the amplitude of $2f_m$ gradually reduces, which indicates that the increase of crack depth will lead to the rising of the sideband amplitude but reduce the amplitude of primary response meshing frequency.

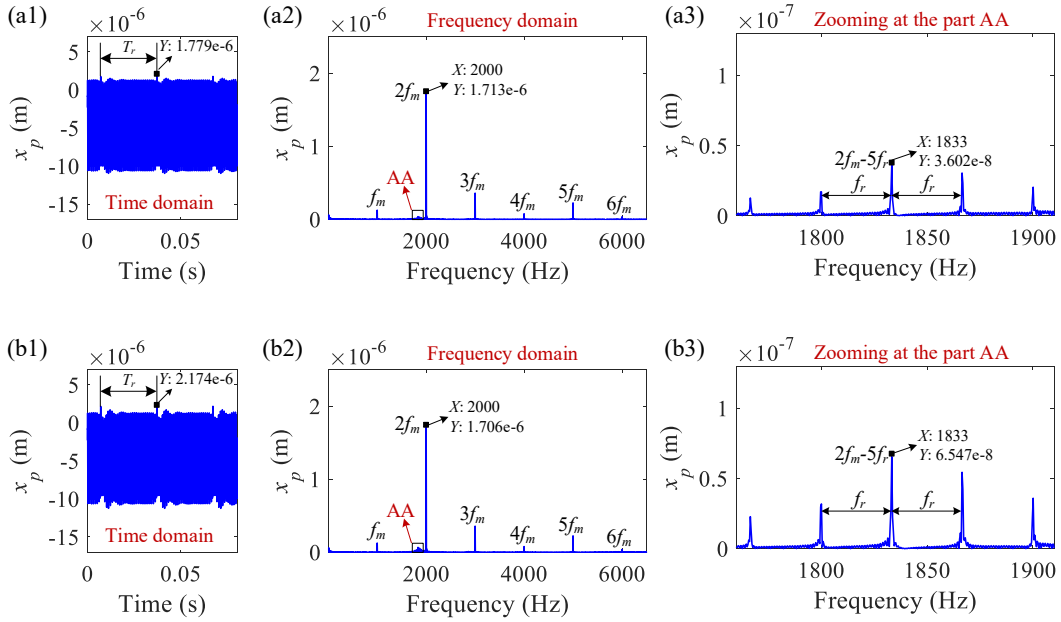

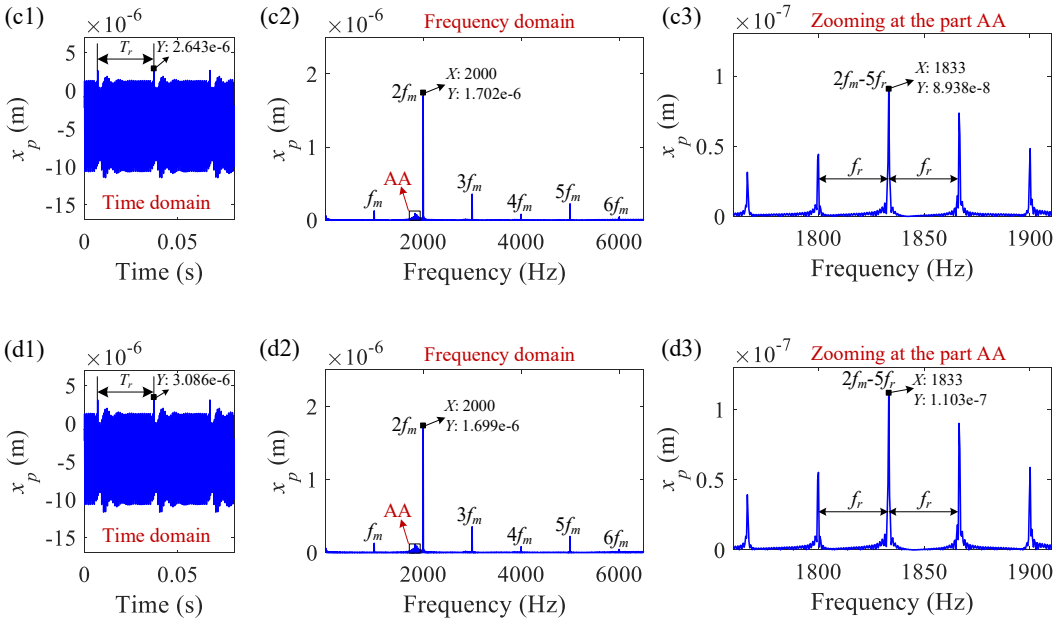

Fig. 23 Time and frequency domain spectra under different body crack depths (v = 15°, T_p = 100 N, C_n = 0.8 and L_n = 0.6): (a) q = 1 mm, (b) q = 2 mm, (c) q = 3 mm, (d) q = 4 mm

The effects of crack propagation on the spectrum characteristic parameters of the body and tooth cracked gears are presented in Fig. 24. It can be found that with the crack growth, the amplitude of $2f_m$ of both the body and tooth cracked gear tends to decrease, except in the tooth crack case q = 4 mm there is a sudden increase, which is because that the tooth crack with depth 4 mm almost broke the gear tooth. From Fig. 24 we can also see that the MASF, SASF and R_{MASF} and R_{SASF} of both the body and tooth crack cases increase with the crack depth extending, but the amplitude of these parameters in the case of tooth crack is significantly greater than that of body crack under the same crack depth, especially in the large crack. The peak position of the sideband is consistently maintained at position $2f_m$-$5f_r$, indicating that the crack angle and depth only affect the amplitude of the sideband but have no effect on the peak position of the sideband.

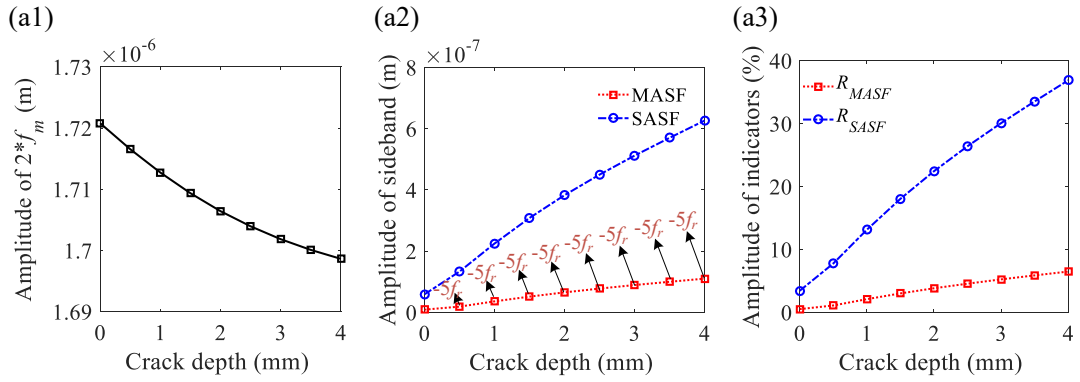

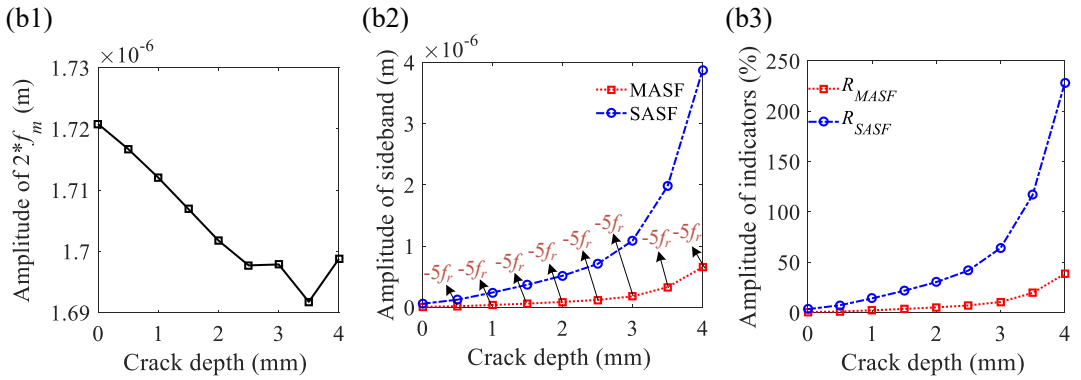

Fig. 24 Effects of crack propagation on frequency spectrum characteristics of cracked gear under different crack types (T_p = 100 N, C_n = 0.8 and L_n = 0.6): (a) body crack (ν = 15°), (b) tooth crack (ν = 75°)

In this study, some well-behaved time domain statistical indicators, such as root mean square (RMS) [6, 26-27, 45-47], kurtosis [6, 26-27, 45, 48-49], crest factor (CF) [6, 26-27, 46-47], Peak [46-47], Sr [45], Sa [45], M6A [6, 46] and M8A [6, 46] are adopted to evaluate the crack propagation status.

Fig. 25 shows the performance of the adopted time-domain statistical indicators of tooth and body cracked gear under different crack propagation depths. In Fig. 25, the ordinate is the ratio of the statistical index at different crack depths to that of the healthy case. It can be clearly seen in Fig. 25 (a1) and (b1) that with the crack propagation, the Peak, M8A, CF, M6A and Kurtosis all increase in the body and tooth crack cases and their amplitudes in tooth crack case is larger than that of the body crack case under the same crack depth. The Peak value shows more sensitivity and robustness to the crack propagation under the two types of crack cases. There is a sharp change in the indicators under the case of tooth crack when the crack becomes larger (q = 3.5 mm and 4 mm), which is because the large tooth crack reduced the TVMS sharply, then leading to the intensification of gear vibration impact.

By comparing Fig. 25 (a2) with (b2), it can be found that with the crack depth increasing, the RMS of both the body and tooth crack cases decrease first and then increase, and the Sr of the two crack cases increase first and then decrease. The variation trend of Sr is consistent with that of Sa, although the decline stage of Sa is not shown in the case of body crack. In general, with the crack propagation, the RMS, Sr and Sa are not much sensitive to the body crack but only to larger tooth crack depths, such as cases q = 3.5 mm and 4 mm in Fig. 25 (b2). This phenomenon indicates that the depth of the crack may have reached a large level and the tooth breaking may occur soon when RMS, Sr and Sa change sharply.

In summary, the indicator Peak is recommended to be used first for the selection of statistical indicators to evaluate the status of both the tooth and body crack propagation, due to its maximum sensitivity in both smaller and larger cracks under two types of cracks. The M8A, M6A and CF with relatively good performance are recommended in the second place. Compared with the body crack, the statistical indicators of tooth crack are prone to abrupt change under the condition of the large crack, especially for the indicators M8A and M6A. This abrupt change characteristic may also be used to evaluate the crack types or the crack angles.

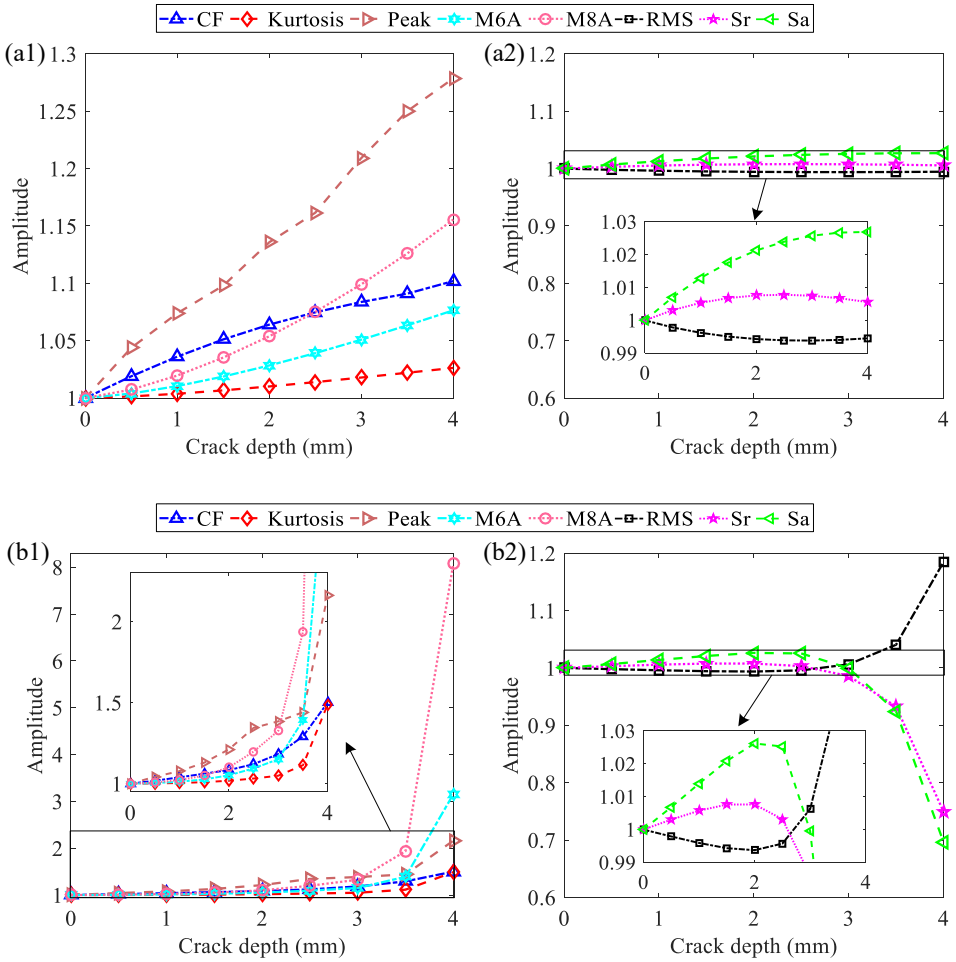

Fig. 25 Performance of time-domain statistical indicators for different crack types : (T_p = 100 N, C_n = 0.8 and L_n = 0.6): (a) body crack (v = 15º), (b) tooth crack (v = 75º)

7 Conclusions

To solve the problem that the traditional analytical TVMS calculation models and dynamic simulations are not applicable to the gear body crack fault case, a new analytical TVMS calculation model of cracked gear with TR is developed based on the proposed VADEI method. Then, the validating study for the effectiveness and accuracy of the proposed TVMS calculation model using the FE method is carried out. On this basis, a dynamic model of the gear system with 6-DOF for the analysis of the crack fault vibration characteristics is established. Finally, the effects of different TVMS calculation models, parameters of TR, load and crack on the TVMS excitation and dynamic characteristics of the gear system are investigated and discussed. Through this study, some conclusions can be drawn as follows:

(1) The calculation results obtained from the FE models agree well with the proposed TVMS calculation model in both the tooth and body crack cases, which indicates the effectiveness, universality and accuracy of the proposed model, as well as the correctness of the proposed VADEI method.

(2) The influence of tooth attachment position change caused by the crack angle on the TVMS is not obvious when the crack is relatively small, while it will become significant in the larger crack case and can not be ignored.

(3) The smaller amount and length of TR and the larger load and crack depths are easily leading to the corner contact of cracked gear. The corner contact phenomenon is more likely to occur in the tooth crack case than in the body crack case under the same crack depth.

(4) Due to not considering the effects of tooth attachment position change caused by the crack, the traditional model will lead to larger TVMS calculation results and smaller vibration responses compared with the real situation, this calculation error will be amplified in the case of body crack.

(5) The TVMS will decrease and the dynamic response will increase with both the tooth and body crack propagation. The effects of tooth crack on the TVMS and dynamic responses are more significant than that of the body crack under the same crack depth.

(6) Different parameters of TR and load will lead to the variation of the phase and amplitude of the TVMS excitation of cracked gear with tooth errors, which will further result in different phase and amplitude modulations caused by the periodic impact of crack fault. This phenomenon is mainly reflected in the changes in the amplitude and peak of the sidebands in the frequency spectrum of cracked gear.

(7) The Peak value is recommended first to be used as the time-domain statistical indicator to evaluate the status of crack propagation due to its good performance in both the tooth and body crack cases. Compared with the body crack, the time- and frequency-domain statistical indicators (such as M8A, M6A, SASF, etc.) for tooth crack are prone to abrupt change under the large crack case, which may be used to evaluate or identify the crack types or crack angles.

It should be pointed out that in our study, only the tooth errors caused by the TR are considered, and the influences of other types of errors, such as manufacturing errors (tooth pitch errors, random tooth profile errors and eccentricity errors, etc.) and installation errors on the internal excitation and vibration of gears need further study. In addition, the proposed TVMS calculation model in this paper can be further extended and applied. For example, the effects of the extended tooth contact [50-51] caused by a heavy load, the coupling deformation of fillet foundation between meshing teeth [19, 52-53] and the nonlinear Hertz contact characteristic between meshing pairs [54-55] on TVMS excitation deserve further consideration to improve the proposed model. Moreover, some fault vibration characteristics or diagnostic indicators obtained based on the theoretical simulation models in this paper will inevitably have a certain deviation from the actual situation. How to use some FE dynamic models [10, 56] or test means to verify and correct the proposed simulation models is worth further research in the later stage.

Acknowledgments

The authors are grateful for the National Natural Science Foundation of China (Grant No. 52035002), the Graduate Research and Innovation Foundation of Chongqing, China (Grant No. CYB21014) and China Scholarship Council (202106050062).

Data availability

The datasets generated and analyzed during the current study are available from the corresponding author on reasonable request.

Declaration of Competing Interest

The authors declare that they have no competing financial interests or personal relationships that could have appeared to influence the work reported in this paper.

References

[1] J. Liu, Z. Xu. A simulation investigation of lubricating characteristics for a cylindrical roller bearing of a high-power gearbox. Tribology International, 2022; 167: 107373.

[2] J. Shi, X. Gou, L. Zhu. Generation mechanism and evolution of five-state meshing behavior of a spur gear system considering gear-tooth time-varying contact characteristics. Nonlinear Dyn. 2021; 106: 2035–2060.

[3] X. Sun, T. Wang, R. Zhang, F. Gu, A. D. Ball. Numerical Modelling of Vibration Responses of Helical Gears under Progressive Tooth Wear for Condition Monitoring. Mathematics. 2021; 9(3): 213.

[4] T. Eritenel, RG. Parker. An investigation of tooth mesh nonlinearity and partial contact loss in gear pairs using a lumped-parameter model. Mech. Mach. Theory. 2014; 76:20–38.

[5] L. M. Wang, Y. M. Shao. Fault feature extraction of rotating machinery using a reweighted complete ensemble empirical mode decomposition with adaptive noise and demodulation analysis. Mech. Syst. Sig. Process. 2020; 138:106545.

[6] Z. Chen, W. Zhai, K. Wang. Vibration feature evolution of locomotive with tooth root crack propagation of gear transmission system. Mech. Syst. Sig. Process. 2019; 115:29–44.

[7] W. Yu, C. K. Mechefske, M. Timusk. Effects of tooth plastic inclination deformation due to spatial cracks on the dynamic features of a gear system. Nonlinear Dyn. 2017; 87: 2643–2659.

[8] Z. Chen, J. Ning, K. Wang, W. Zhai. An improved dynamic model of spur gear transmission considering coupling effect between gear neighboring teeth. Nonlinear Dyn. 2021; 106: 339–357.

[9] X, Liang, M. Zuo, M. Pandey. Analytically evaluating the influence of crack on the mesh stiffness of a planetary gear set. Mech Mach Theory. 2014; 76(1):20–38.

[10] Y. Huangfu, K. Chen, H. Ma, X. Li, H. Han, Z. Zhao. Meshing and dynamic characteristics analysis of spalled gear systems: A theoretical and experimental study. Mech. Syst. Sig. Process. 2020; 139:106640.

[11] Y. Luo, N. Baddour, M. Liang. A shape-independent approach to modelling gear tooth spalls for time varying mesh stiffness evaluation of a spur gear pair. Mech. Syst. Sig. Process, 2019; 120:836–852.

[12] G. Liu, J. Hong, R. G. Parker. Influence of simultaneous time-varying bearing and tooth mesh stiffness fluctuations on spur gear pair vibration. Nonlinear Dyn. 2019; 97: 1403–1424.

[13] X. Liang, H. Zhang, M. Zuo, Y. Qin. Three new models for evaluation of standard involute spur gear mesh stiffness, Mech. Syst. Sig. Process. 2018; 101: 424–434.

[14] A. Fernandez, M. Iglesias, A. De-Juan, P. García, R. Sancibrián, F.Viadero. Gear transmission dynamic: Effects of tooth profile deviations and support flexibility. Applied Acoustics, 2014; 77:138–149.

[15] H. Ma, X. Pang, R. Feng, J. Zeng, B. Wen. Improved time-varying mesh stiffness model of cracked spur gears. Eng. Fail. Anal. 2015, 55: 271–287.

[16] Y. Pandya, A, Parey. Experimental investigation of spur gear tooth mesh stiffness in the presence of crack using photoelasticity technique. Eng. Fail. Anal. 2013; 34: 488–500.

[17] N. Raghuwanshi, A. Parey. A New Technique of Gear Mesh Stiffness Measurement Using Experimental Modal Analysis. Journal of vibration and acoustics. 2018; 141(2).

[18] O. Mohammed, M. Rantatalo. Gear fault models and dynamics-based modelling for gear fault detection–A review. Eng. Fail. Anal. 2020; 117: 104798.

[19] C. Xie, X. Shu. A new mesh stiffness model for modified spur gears with coupling tooth and body flexibility

effects. Applied Mathematical Modelling. 2020; 91: 1194–1210.
[20] H. Jiang, F. Liu, M. Wang. Dynamic Simulation of Helical Gears with Crack Propagating In to Gear Body. IOP Conference Series Earth and Environmental Science. 2020; 440: 022108.
[21] D. G. Lewicki. Effect of rim thickness on gear crack propagation path. J. Mech. Des. 1997; 119:88–95.
[22] S. Zouari, M. Maatar, T. Fakhfakh. Following Spur Gear Crack Propagation in the Tooth Foot by Finite Element Method. J Fail. Anal. and Preven. 2010; 10: 531–539.
[23] M. HaddarZ. Wan, H. Cao, Y. Zi, W. He, Z. He. An improved time-varying mesh stiffness algorithm and dynamic modeling of gear-rotor system with tooth root crack. Eng. Fail. Anal. 2014; 42: 157–77.
[24] F. Zhao, Z. Tian, Y. Zeng. Uncertainty quantification in gear remaining useful life prediction through an integrated prognostics method. IEEE Trans Reliab. 2013; 62:146–59.
[25] Y. Jiang, H. Zhu, Z. Li. The nonlinear dynamics response of cracked gear system in a coal cutter taking environmental multi-frequency excitation forces into consideration. Nonlinear Dyn. 2016; 84: 203–222.
[26] O. Mohammed, M. Rantatalo, J. Aidanpaa. Improving mesh stiffness calculation of cracked gears for the purpose of vibration-based fault analysis. Eng. Fail. Anal. 2013; 34: 235–251.
[27] Z. Chen, W. Zhai, Y. Shao, K. Wang, G. Sun. Analytical model for mesh stiffness calculation of spur gear pair with non-uniformly distributed tooth root crack. Eng. Fail. Anal. 2016; 66: 502–514.
[28] H. Ma, R. Song, X. Pang, B. Wen. Time-varying mesh stiffness calculation of cracked spur gears. Eng. Fail. Anal. 2014; 44:179–94.
[29] Z. Chen, Y. Shao. Dynamic simulation of spur gear with tooth root crack propagating along tooth width and crack depth. Eng. Fail. Anal. 2011; 18: 2149–2164.
[30] L. Yang, L.Wang, Y. Shao, C. K. Mechefske, Q. Chen. A new calculation method for tooth fillet foundation stiffness of cracked spur gears. Eng. Fail. Anal. 2021, 121(3): 105173.
[31] H. Ma, J. Zeng, R. Feng, P. Xu, B. Wang, B. Wen. Review on dynamics of cracked gear systems. Eng. Fail. Anal. 2015; 55: 224–245.
[32] Z. Chen, J. Zhang, W. Zhai, Y. Wang, J. Liu. Improved analytical methods for calculation of gear tooth fillet-foundation stiffness with tooth root crack. Eng. Fail. Anal. 2017; 82: 72–81.
[33] X. Zhou, Y. Shao. Time-varying meshing stiffness calculation and vibration analysis for a 16 degree of dynamic model with linear crack growth in a pinion. J. Sound Vib. 2012; 134: 011011.
[34] H. Ma, X. Feng, R. Song, J. Yang. Time-Varying Mesh Stiffness Calculation of Spur Gears Based on Improved Energy Method. Journal of Northeastern University (Natural Science). 2014; 35(6): 863.
[35] H. Ma, X. Pang, J. Zeng, Q. Wang, B. Wen. Effects of gear crack propagation paths on vibration responses of the perforated gear system. Mech. Syst. Sig. Process. 2015; 62: 113–128.
[36] P. Liu, L. Zhu, X. Gou, J. Shi, G. Jin. Neighboring periodic motion in spur gear pair and its identification methods. Nonlinear Dyn. 2021; 106: 2991–3023.
[37] L. Yang, Q. Chen, L. Yin, L. Wang, Y. Shao. Dynamic characteristic of spur gear system with spalling fault considering tooth pitch error. Qual. Reliab. Eng. Int. 2021; 1–18.
[38] Z. Chen, Y. Shao. Mesh stiffness calculation of a spur gear pair with tooth profile modification and tooth root crack. Mech. Mach. Theory. 2013; 62: 63–74.
[39] L. Yang, L. Wang, W. Yu, Y. Shao. Investigation of tooth crack opening state on time varying meshing stiffness and dynamic response of spur gear pair. Eng. Fail. Anal. 2021; 121(8):105181.
[40] D. C. H. Yang, J. Y. Lin. Hertzian damping, tooth friction and bending elasticity in gear impact dynamics. Journal of Mechanisms, Transmissions, and Automation. 1987;109(2): 189–196.
[41] X. Tian. Dynamic Simulation for System Response of Gearbox Including Localized Gear Faults. University of Alberta, Edmonton, Alberta, Canada, 2004 (Master's Thesis).

[42] D. Yang, Z. Sun. A rotary model for spur gear dynamics. ASME J Mech Trans Aut Des. 1985; 107:529–535.
[43] P. Sainsot, P. Velex, O. Duverger. Contribution of gear body to tooth deflections – a new bidimensional analytical formula. Journal of Mechanical Design –ASME. 2004; 126(4): 748–752.
[44] X. Ding; Q. He, Y. Shao, W. Huang. Transient Feature Extraction Based on Time-Frequency Manifold Image Synthesis for Machinery Fault Diagnosis. IEEE Trans. Instrum. Meas. 2019; 68, 1–14.
[45] S. Wu, M. Zuo, A. Parey. Simulation of spur gear dynamics and estimation of fault growth. J. Sound Vib. 2008; 317 (3–5): 608–624.
[46] V. Sharma, A. Parey. A review of gear fault diagnosis using various condition indicators. Procedia Eng. 2016; 144: 253–263.
[47] Y. Yang, W. Xia, J. Han, Y. Song, J. Wang, Y. Dai. Vibration analysis for tooth crack detection in a spur gear system with clearance nonlinearity. Int. J. Mech. Sci. 2019; 157: 648–661.
[48] B. Chen, W. Zhang, D. Song, Y. Cheng. Blind deconvolution assisted with periodicity detection techniques and its application to bearing fault feature enhancement. Measurement. 2020; 159: 107804.
[49] B. Chen, Y. Cheng, W. Zhang, F. Gu. Investigations on improved Gini indices for bearing fault feature characterization and condition monitoring. Mech. Syst. Sig. Process. 2022; 176: 109165.
[50] H. Ma, X. Pang, R. Feng, R. Song, B. Wen. Fault features analysis of cracked gear considering the effects of the extended tooth contact. Eng. Fail. Anal. 2015; 48:105–20.
[51] W. Yu, C. K. Mechefske. Analytical modeling of spur gear corner contact effects. Mech. Mach. Theory. 2016; 96 :146–164.
[52] C. Xie, L. Hua, X. Han, J. Lan, X. Wan, X. Xiong. Analytical formulas for gear body-induced tooth deflections of spur gears considering structure coupling effect. Int. J. Mech. Sci. 2018; 148: 174–190.
[53] Z. Chen, Z. Zhou, W. Zhai, K. Wang. Improved analytical calculation model of spur gear mesh excitations with tooth profile deviations - ScienceDirect. Mech. Mach. Theory. 2020; 149: 103838.
[54] M. Sánchez, M. Pleguezuelos, J. Pedrero. Approximate equations for the meshing stiffness and the load sharing ratio of spur gears including hertzian effects. Mech. Mach. Theory. 2017; 109: 231–249.
[55] Z. Cao, Z. Chen, H. Jiang. Nonlinear dynamics of a spur gear pair with force-dependent mesh stiffness. Nonlinear Dyn. 2020; 99: 1227–1241.
[56] K. Chen, Y. Huangfu, Z. Zhao, H. Ma, X. Dong. Dynamic modeling of the gear-rotor systems with spatial propagation crack and complicated foundation structure. Mech. Mach. Theory. 2022, 172: 104827.